
Towards Evaluating the Robustness of Visual State Space Models

Hashmat Shadab Malik
MBZUAI, UAE

Fahad Shamshad
MBZUAI, UAE

Muzammal Naseer
MBZUAI, UAE

Karthik Nandakumar
MBZUAI, UAE

Fahad Shahbaz Khan
MBZUAI, UAE
Linköping University

Salman Khan
MBZUAI, UAE
ANU, Australia

{firstname.lastname}@mbzuai.ac.ae

Abstract

Vision State Space Models (VSSMs), a novel architecture that combines the strengths of recurrent neural networks and latent variable models, have demonstrated remarkable performance in visual perception tasks by efficiently capturing long-range dependencies and modeling complex visual dynamics. However, their robustness under natural and adversarial perturbations remains a critical concern. In this work, we present a comprehensive evaluation of VSSMs' robustness under various perturbation scenarios, including occlusions, image structure, common corruptions, and adversarial attacks, and compare their performance to well-established architectures such as transformers and Convolutional Neural Networks. Furthermore, we investigate the resilience of VSSMs to object-background compositional changes on sophisticated benchmarks designed to test model performance in complex visual scenes. We also assess their robustness on object detection and segmentation tasks using corrupted datasets that mimic real-world scenarios. To gain a deeper understanding of VSSMs' adversarial robustness, we conduct a frequency analysis of adversarial attacks, evaluating their performance against low-frequency and high-frequency perturbations. Our findings highlight the strengths and limitations of VSSMs in handling complex visual corruptions, offering valuable insights for future research and improvements in this promising field. Our code and models will be available at <https://github.com/HashmatShadab/MambaRobustness>.

1 Introduction

Deep learning models such as Convolutional Neural Networks (CNNs) [23] and Vision Transformers [9] have achieved remarkable success across various visual perception tasks, including image classification, object detection, and semantic segmentation. However, their robustness across different distribution shifts of the data remains a significant concern for their deployment in security-critical applications. Several works [17, 49, 37, 2] have extensively evaluated the robustness of CNNs and Transformers against common corruptions, domain shifts, information drop, and adversarial attacks, highlighting that a model's design impacts its ability to handle adversarial and natural corruptions, with robustness varying across different architectures. This observation motivates us to investigate the robustness of the recently proposed Vision State-Space Models (VSSMs) [50, 28, 14], a novel architecture designed to efficiently capture long-range dependencies in visual data.

CNNs are particularly adept at extracting hierarchical image features due to their shared weights across features, which help in capturing local-level information. In contrast, transformer-based

models employ an attention mechanism that captures global information, effectively increasing the model’s receptive field [9]. This allows transformers to excel at modeling long-range dependencies. However, a significant drawback of transformers is their quadratic computational scaling with input size, which makes them computationally expensive for downstream tasks [31]. Recently, state space sequence models (SSMs) have been adapted from the natural language domain to vision tasks. Unlike transformers, vision-based SSMs offer the capability to handle long-range dependencies while maintaining a linear computational cost, providing a more efficient alternative for vision applications [15, 14, 28, 50, 25, 4].

VSSMs, such as the Vision Mamba [14] and VMamba [28] models, have gained attention in the vision domain due to their impressive performance. These models offer a unique approach to managing spatial dependencies, which is critical for handling dynamic visual environments. Their ability to selectively adjust interactions between states promises enhanced adaptability, a trait that could be pivotal in improving resilience against perturbations. Given their potential in safety-critical applications such as autonomous vehicles, robotics, and healthcare, it is crucial to thoroughly assess the robustness of these models.

In this paper, we present a comprehensive analysis of the performance of VSSMs, Vision Transformers, and CNNs in handling various nuisances for classification, detection, and segmentation tasks, aiming to provide valuable insights into their robustness and suitability for real-world applications. Our evaluation is divided into three main parts, each addressing a crucial aspect of model robustness.

- 1 **Occlusions and Information Loss:** We rigorously assess the robustness of VSSMs against information loss along scanning directions and severe occlusions affecting foreground objects, non-salient background regions, and random patch drops at multiple levels. This analysis is crucial for understanding how well VSSMs can handle partial information drop and maintain performance despite occlusions. Additionally, we explore the sensitivity of VSSMs to the overall image structure and global composition through patch shuffling experiments, providing insights into their ability to capture and utilize global context.

Findings: Our experiments reveal that ConvNext [30] and VSSM models are superior in handling of sequential information loss along the scanning direction compared to ViT and Swin models. In scenarios involving random, salient, and non-salient patch drops, VSSMs exhibit the highest overall robustness, although Swin models perform better under extreme information loss. Additionally, VSSM models show greater resilience to spatial structure disturbances caused by patch shuffling compared to Swin models.

- 2 **Common Corruptions:** We evaluate the robustness of VSSM-based classification models against common corruptions that mimic real-world scenarios. This includes both *global corruptions* such as noise, blur, weather, and digital-based corruptions at multiple intensity levels, and *fine-grained corruptions* like object attribute editing and background manipulations. Furthermore, we extend the evaluation to VSSM-based detection and segmentation models to demonstrate their robustness in dense prediction tasks. By testing the models under these diverse and challenging conditions, we aim to provide a comprehensive understanding of their performance and resilience in real-world applications.

Findings: For global corruptions, VSSM models experience the least average performance drop compared to Swin and ConvNext models. When subjected to fine-grained corruptions, the VSSM family outperforms all transformer-based variants and maintains performance that is either better than or comparable to the advanced ConvNext models. In dense prediction tasks such as detection and segmentation, VSSM-based models generally demonstrate greater resilience and outperform other models.

- 3 **Adversarial Attacks:** We analyze the robustness of VSSMs against adversarial attacks in both white-box and black-box settings. In addition to the standard adversarial evaluation, we conduct a frequency analysis to demonstrate the resilience of VSSM models against low-frequency and high-frequency adversarial perturbations. This analysis provides insights into VSSMs ability to withstand adversarial perturbations at different frequency levels.

Findings: For adversarial attacks, smaller VSSM models exhibit higher robustness against white-box attacks compared to their Swin Transformer counterparts, although this robustness does not scale to the larger VSSM model. VSSM models maintain robustness above 90% for low-frequency perturbations even under large perturbation strengths, but their performance deteriorates rapidly with high-frequency perturbation attacks. For standard attacks across

the full frequency range, VSSM models demonstrate greater robustness against attacks with smaller perturbation budgets compared to ConvNext, ViT, and Swin models. In adversarial fine-tuning, VSSM models show strong performance for high-resolution images in both clean and robust accuracy. However, for low-resolution datasets like CIFAR-10, transformer-based ViT models outperform Mamba-based VSSM models.

Our findings highlight the strengths and limitations of VSSM models in handling various nuisances and adversarial attacks. While VSSMs demonstrate superior robustness in many scenarios, there are areas where other architectures, such as ConvNext and ViT, exhibit competitive or even better performance. These insights can guide researchers and practitioners in selecting the most appropriate model for their specific applications, taking into account the potential challenges and requirements for robustness in real-world settings.

2 Related Work

Robustness of Deep Learning Models: Robustness refers to a conventionally trained model’s ability to maintain satisfactory performance under natural and adversarial distribution shifts [12, 10]. In practice, deep learning-based models often encounter various types of corruptions, such as noise, blur, compression artifacts, and adversarial perturbations, which can significantly degrade their performance. To ensure the reliability and robustness of these models, it is essential to systematically evaluate their performance under such challenging conditions. Recent studies have investigated the robustness of deep learning-based models across a wide range of areas, including image classification [17, 19], semantic segmentation [21], object detection [36], video classification [45], point cloud processing [20], and transformer-based architectures [39, 24, 40]. However, there is a lack of similar investigations for vision state space models (VSSMs), despite their growing popularity and potential applications [27, 46, 44, 6]. In this work, we aim to bridge this gap by examining how the performance of VSSMs is affected by adversarial and common corruptions, thereby contributing to a more comprehensive understanding of model robustness across different architectural paradigms. Considering the increasing adoption of VSSMs, our findings can provide valuable insights for researchers and practitioners working on developing robust and reliable vision systems.

State Space Models: State space models (SSMs) [35, 42] have emerged as a promising method for modeling sequential data in deep learning. These models map a 1-dimensional sequence $x(t) \in \mathbb{R}^L$ to $y(t) \in \mathbb{R}^L$ via an implicit latent state $h(t) \in \mathbb{R}^N$ as:

$$h'(t) = Ah(t) + Bx(t), \quad y(t) = Ch(t), \quad (1)$$

where $A \in \mathbb{R}^{N \times N}$, $B \in \mathbb{R}^{N \times 1}$, and $C \in \mathbb{R}^{N \times 1}$ are continuous parameters governing the dynamics and output mapping. To enhance computational efficiency, the continuous SSM is discretized using a zero-order hold assumption, leading to a discretized form:

$$h_t = \bar{A}h_{t-1} + \bar{B}x_t, \quad y_t = Ch_t, \quad (2)$$

where \bar{A} and \bar{B} are the discrete counterparts of A and B , obtained via a specified sampling timescale $\Delta \in \mathbb{R} > 0$. The iterative process in Eq. 2 can be further expedited through parallel computation using a global convolution operation:

$$y = x \circledast \bar{K}, \quad \text{with } \bar{K} = (C\bar{B}, C\bar{A}\bar{B}, \dots, C\bar{A}^{L-1}\bar{B}), \quad (3)$$

where $\bar{K} \in \mathbb{R}^L$ is the kernel used and \circledast denotes convolution operator. Recent advancements in SSMs, such as the Mamba models [14], address the limitations of fixed parameterization by introducing a dynamic and selective approach for managing interactions between sequential states. Mamba utilizes input-dependent parameters, enabling more complex and sequence-aware parameterization. These capabilities have inspired the development of new models in vision tasks, such as VMamba [28], which integrate Mamba with ViT-like hierarchical models. Although these architectures have been extensively investigated for various vision tasks, including detection, segmentation, and restoration, their robustness against natural and adversarial corruptions remains relatively less explored. In this work, we aim to extensively evaluate the resilience of these state-space-based vision models against natural and adversarial perturbations, which is crucial for understanding their potential in real-world applications and identifying areas for improvement.

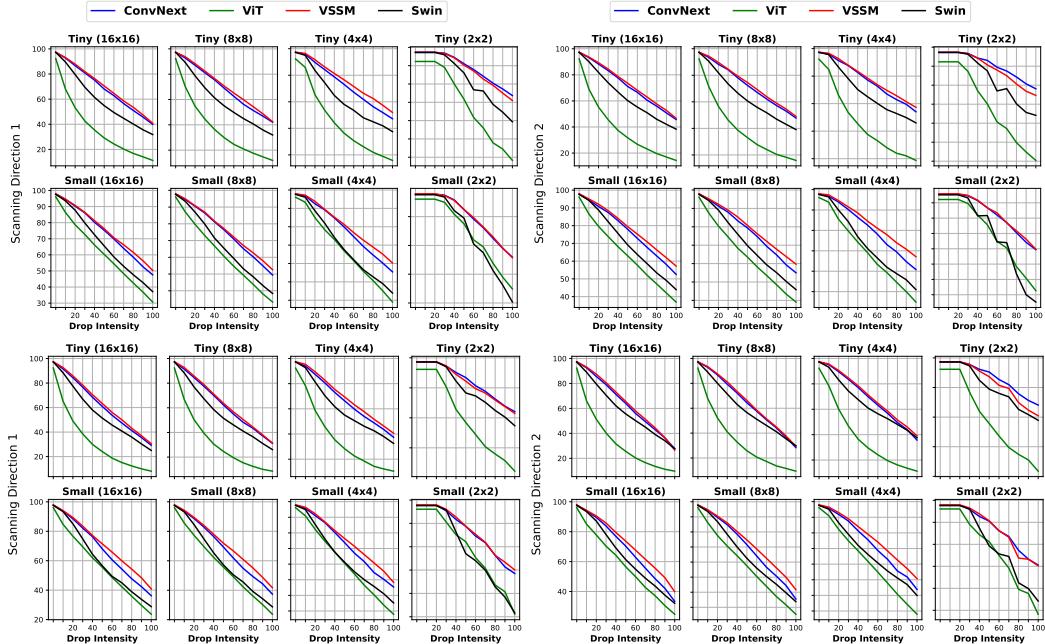


Figure 1: Information drop of Tiny and Small family of models along the scanning direction: the image is split into a sequence of fixed-size non-overlapping patches of size 16x16, 8x8, 4x4, and 2x2. The top two rows show the results of linearly increasing the number of pixels dropped from each patch to the maximum threshold (*Drop Intensity*) along the scanning direction. The bottom two rows present results of linearly increasing the number of pixels dropped from each patch to the maximum threshold (*Drop Intensity*) until the center of the scanning direction. The plots on the left show results for top-to-bottom direction, while those on the right show results for left-to-right direction. More detailed analysis is provided in Section B.1 of Appendix.

3 Robustness Evaluation of Vision State Space Models

We have broadly categorized the experiments into natural and adversarial corruption categories to evaluate the robustness of CNNs, transformers, and VSSMs across tiny, small, and base-model families. For natural corruptions, we conduct experiments on classification, detection, and segmentation tasks. For the classification task, we employ the recent ConvNext model [30] as a representative of the CNN family, while selecting the ViT [9] and Swin [29] family models for transformer architectures. For VSSMs, we report results on VMamba v2 pretrained models [28]. For detection and segmentation, we report results using ImageNet-pretrained backbones of the specified models. These models are fine-tuned with the MMDetection [5] and MMSegmentation [7] frameworks. For detection, we utilize Mask-RCNN [16], and for segmentation, we use UperNet [43] as the network architecture. To evaluate the robustness of VSSMs against adversarial attacks, we consider imagenet trained classification models. Furthermore, we use imagenet pretrained models for adversarial fine-tuning on two downstream datasets; CIFAR-10 [22] and Imagenette [1]. All the evaluations for the task of classification are done on image size of 224×224 , except for CIFAR-10 where image size of 32×32 is used. For detection and segmentation, evaluation is done on image size of 800×1216 and 512×512 , respectively.

3.1 Robustness against Natural Corruptions

We categorize natural corruptions into **information drop** and **ImageNet-based corruption benchmarks**. Information drop experiments assess models’ robustness against various patch perturbations, such as occlusions, random patch drops, and patch shuffling, assessing their ability to handle partial information loss and local distortions. All information drop experiments are conducted on 5000 images from the ImageNet validation set, following [38]. ImageNet-based corruptions, on the other hand, are standard benchmarks that mimic real-world corruptions, including noise, blur, weather, background change, and digital-based corruptions at multiple intensity levels. We also demonstrate the robustness of **VSSM-based detectors and segmentation models** under natural corruptions.

Table 1: Top-1 classification accuracy of various architectures under random patch drop occlusions.

| ResNet-50 | ConvNext-T | ConvNext-S | ConvNext-B | ViT-T | ViT-S | ViT-B | VSSM-T | VSSM-S | VSSM-B | Swin-T | Swin-S | Swin-B |
|---|------------|------------|------------|-------|-------|-------|--------|--------|--------|--------|--------|--------|
| Patch Size 16×16 (Percentage of patch drop increasing from top to bottom (10% to 90%)) | | | | | | | | | | | | |
| 96.70 | 97.24 | 97.78 | 97.84 | 92.30 | 96.08 | 97.54 | 97.38 | 97.94 | 97.96 | 97.24 | 97.60 | 97.60 |
| 75.27 | 96.49 | 97.19 | 97.37 | 90.83 | 95.39 | 96.85 | 96.49 | 96.61 | 97.25 | 96.76 | 97.38 | 97.32 |
| 39.93 | 94.63 | 95.27 | 96.48 | 88.09 | 94.29 | 96.27 | 95.16 | 92.97 | 96.25 | 96.11 | 96.84 | 96.79 |
| 17.91 | 89.99 | 91.12 | 95.29 | 85.26 | 92.35 | 95.08 | 93.45 | 89.74 | 95.21 | 94.88 | 95.88 | 96.17 |
| 6.73 | 81.43 | 84.63 | 93.03 | 80.08 | 90.15 | 92.78 | 90.52 | 84.82 | 93.46 | 93.38 | 94.35 | 95.03 |
| 2.43 | 70.07 | 74.44 | 88.76 | 72.49 | 85.10 | 89.21 | 86.52 | 78.41 | 90.89 | 91.05 | 92.21 | 93.25 |
| 1.05 | 57.59 | 60.15 | 82.35 | 61.34 | 76.56 | 82.08 | 80.52 | 68.40 | 87.03 | 87.96 | 87.84 | 90.43 |
| 0.56 | 44.67 | 44.71 | 71.25 | 45.63 | 62.63 | 70.25 | 70.39 | 52.72 | 79.96 | 80.65 | 79.71 | 84.70 |
| 0.45 | 31.29 | 28.82 | 57.71 | 25.86 | 41.73 | 50.08 | 56.23 | 34.51 | 67.56 | 70.37 | 66.60 | 74.38 |
| 0.43 | 16.73 | 14.98 | 33.67 | 7.85 | 15.86 | 19.68 | 34.83 | 16.82 | 41.55 | 47.16 | 47.85 | 53.54 |
| Patch Size 8×8 (Percentage of patch drop increasing from top to bottom (10% to 90%)) | | | | | | | | | | | | |
| 96.70 | 97.24 | 97.78 | 97.84 | 92.32 | 96.08 | 97.54 | 97.38 | 97.94 | 97.96 | 97.24 | 97.60 | 97.60 |
| 44.91 | 86.69 | 91.39 | 95.63 | 70.18 | 88.90 | 94.23 | 87.86 | 85.93 | 90.20 | 96.44 | 96.77 | 96.76 |
| 12.44 | 68.38 | 81.13 | 90.83 | 42.19 | 79.72 | 88.37 | 79.91 | 78.23 | 84.43 | 95.04 | 94.87 | 95.84 |
| 3.79 | 55.12 | 68.35 | 84.08 | 16.91 | 65.39 | 76.63 | 70.40 | 70.95 | 78.47 | 92.87 | 92.08 | 94.49 |
| 1.35 | 39.05 | 54.58 | 73.51 | 4.59 | 46.17 | 60.12 | 57.34 | 59.09 | 70.04 | 90.13 | 88.21 | 92.40 |
| 0.56 | 23.89 | 37.94 | 58.05 | 1.25 | 25.91 | 39.97 | 43.09 | 44.08 | 58.29 | 85.40 | 81.87 | 88.36 |
| 0.33 | 13.33 | 21.97 | 40.37 | 0.45 | 11.03 | 21.56 | 28.25 | 27.85 | 43.00 | 78.76 | 71.63 | 81.85 |
| 0.21 | 5.95 | 9.85 | 21.51 | 0.21 | 3.78 | 8.85 | 14.69 | 12.45 | 25.75 | 68.40 | 53.81 | 70.03 |
| 0.24 | 2.08 | 2.31 | 7.85 | 0.14 | 1.02 | 2.49 | 5.11 | 2.45 | 10.07 | 52.41 | 29.58 | 49.35 |
| 0.25 | 0.46 | 0.56 | 1.33 | 0.16 | 0.39 | 0.59 | 0.75 | 0.43 | 1.65 | 28.46 | 8.32 | 23.67 |

3.1.1 Robustness against Information Drop

Information Drop along the Scanning Axis: VSSM models scan through input image patches sequentially along four distinct paths in order to capture the spatial information present in the image. These four paths comprise of scanning input patches in the directions of top to bottom, bottom to top, left to right, and right to left. To study the effectiveness of 2D-Selective Scan operation of VSSM model in aggregating the spatial information, we investigate the models’ behavior when information is dropped along the scanning directions. We consider two settings: (1) linearly increasing the amount of information dropped in each patch along the scanning direction, with the most information dropped in patches that are traversed last by the scanning operation, and (2) linearly increasing the amount of information dropped in patches from the start, reaching a maximum at the center, and then linearly decreasing the amount of information dropped until the end.

We split the image into $n \times n$ non-overlapping patches and perform the information drop experiments, with the maximum drop in a patch (*Drop Intensity*) varying from 10% to 100%. In Fig. 1 we report results on information drop along top-to-bottom (*Direction 1*) and left-to-right (*Direction 2*) scanning directions. For both settings (1) and (2) we observe that both ConvNext and VSSM models show high robustness to sequential information drop across various thresholds. Overall, VSSM-T and VSSM-S models demonstrate superior performance compared to their Swin and ViT counterparts across different patch sizes. Pure transformer-based ViT models show poor performance in this experimental setup. We also observe that as we reduce the patch size for splitting the image, leading to a gradual loss of information in the scanning direction, the performance of all the models improves. This implies that handling more abrupt information loss in fewer and larger patches is challenging for these models. In Section B.1 of Appendix, we expand the analysis across base models and all the scanning directions with varying number of patch sizes. **Overall, we observe both ConvNext and VSSM are more adept at handling sequential drop of information along different scanning directions, compared to ViT and Swin Models.**

Random Patch Drop: We assess the robustness of VSSMs in occluded scenarios by randomly dropping patches from images. We split the image into $n \times n$ patches and randomly select patches whose values will be set to zero. As shown in Tab.1 (*top*), when image is split into 16×16 patches, VSSMs consistently outperform ResNet, ConvNext, and ViT models in maintaining accuracy with increasing numbers of dropped patches. However, under conditions of extreme spatial information loss, Swin models demonstrate superior performance. **This trend persists when the image is split into 8×8 patches, as illustrated in Tab.1 (*bottom*), highlighting the robustness of VSSMs and the exceptional resilience of Swin models in extreme patch drop scenarios.** Results on different patch sizes showing similar trend are reported in Appendix B.4.

Table 2: Top-1 classification accuracy reported under salient patch drop occlusion and patch shuffling.

| ResNet-50 | ConvNext-T | ConvNext-S | ConvNext-B | ViT-T | ViT-S | ViT-B | VSSM-T | VSSM-S | VSSM-B | Swin-T | Swin-S | Swin-B |
|--|------------|------------|------------|-------|-------|-------|--------|--------|--------|--------|--------|--------|
| Salient Patch Drop (<i>Percentage of patch drop from top to bottom(10% to 100%)</i>) | | | | | | | | | | | | |
| 92.70 | 96.88 | 97.38 | 97.50 | 90.46 | 95.36 | 94.90 | 97.04 | 97.66 | 97.40 | 96.94 | 97.44 | 97.26 |
| 84.86 | 95.98 | 96.98 | 96.86 | 88.62 | 94.56 | 93.92 | 96.58 | 96.98 | 97.14 | 96.14 | 97.02 | 96.90 |
| 73.64 | 94.60 | 95.86 | 96.52 | 85.40 | 92.70 | 92.52 | 95.34 | 95.82 | 96.74 | 95.02 | 96.22 | 96.24 |
| 60.16 | 92.52 | 94.04 | 94.92 | 80.94 | 89.82 | 89.72 | 93.88 | 93.14 | 95.04 | 93.28 | 94.92 | 94.76 |
| 44.78 | 88.22 | 90.06 | 92.60 | 75.12 | 85.26 | 85.34 | 91.04 | 89.64 | 92.74 | 90.24 | 92.74 | 92.98 |
| 29.16 | 81.40 | 84.02 | 88.64 | 65.42 | 78.06 | 78.36 | 86.34 | 83.66 | 89.30 | 86.76 | 88.88 | 89.78 |
| 16.12 | 72.32 | 74.64 | 82.36 | 51.60 | 67.60 | 68.34 | 79.24 | 74.26 | 83.44 | 80.32 | 82.08 | 83.54 |
| 7.38 | 56.96 | 58.28 | 69.44 | 35.10 | 50.18 | 50.80 | 66.42 | 59.26 | 72.88 | 68.84 | 71.18 | 73.30 |
| 2.14 | 33.80 | 34.96 | 46.52 | 14.96 | 24.26 | 24.72 | 43.90 | 35.38 | 50.94 | 46.42 | 49.58 | 51.80 |
| 0.10 | 0.10 | 0.10 | 0.10 | 0.10 | 0.10 | 0.10 | 0.10 | 0.10 | 0.10 | 0.10 | 0.10 | 0.10 |
| Patch Shuffling (<i>From top to bottom, the image is split into 4, 8, 16, 32, 64, and 256 patches</i>) | | | | | | | | | | | | |
| 90.79 | 95.62 | 96.57 | 96.69 | 85.71 | 92.88 | 95.18 | 95.75 | 96.73 | 96.88 | 95.41 | 96.05 | 96.31 |
| 82.01 | 93.61 | 94.81 | 95.43 | 78.67 | 88.81 | 92.55 | 94.66 | 95.75 | 96.12 | 93.99 | 94.55 | 95.25 |
| 67.09 | 89.99 | 91.66 | 93.05 | 67.95 | 81.22 | 87.88 | 91.65 | 93.26 | 94.27 | 90.69 | 91.93 | 92.77 |
| 33.34 | 80.29 | 82.06 | 85.31 | 42.65 | 63.97 | 75.68 | 85.34 | 87.10 | 90.08 | 85.01 | 86.33 | 88.18 |
| 10.93 | 63.33 | 64.75 | 69.44 | 19.05 | 45.21 | 55.52 | 73.72 | 73.68 | 80.79 | 76.60 | 75.46 | 80.10 |
| 1.07 | 7.57 | 5.45 | 8.02 | 1.00 | 3.14 | 5.00 | 15.45 | 13.83 | 22.50 | 25.79 | 12.83 | 21.08 |

Table 3: Corruption Error (CE) of various architectures on ImageNet-C corruptions over multiple intensity levels. Results are relative to the CE on ResNet-50 and are evaluated on 5000 ImageNet validation set images.

| Corruptions ↓ | ResNet-50 | ConvNext-T | ConvNext-S | ConvNext-B | ViT-T | ViT-S | ViT-B | VSSM-T | VSSM-S | VSSM-B | Swin-T | Swin-S | Swin-B |
|-------------------|-----------|------------|------------|------------|--------|--------|--------|--------|--------|--------|--------|--------|--------|
| Brightness | 100.00 | 68.20 | 58.63 | 52.15 | 223.14 | 101.09 | 41.67 | 61.60 | 53.06 | 52.94 | 75.89 | 65.35 | 63.54 |
| Contrast | 100.00 | 40.14 | 30.29 | 28.96 | 426.29 | 186.49 | 103.16 | 38.17 | 30.02 | 27.70 | 44.41 | 42.09 | 41.70 |
| Defocus Blur | 100.00 | 85.70 | 77.82 | 73.87 | 103.27 | 70.64 | 42.81 | 84.96 | 72.32 | 73.00 | 87.50 | 66.82 | 81.49 |
| Elastic Transform | 100.00 | 81.11 | 72.18 | 69.44 | 70.34 | 55.69 | 41.43 | 82.78 | 69.89 | 72.21 | 86.36 | 66.53 | 76.78 |
| Fog | 100.00 | 113.68 | 86.18 | 91.19 | 312.26 | 119.54 | 68.79 | 87.47 | 64.93 | 55.88 | 84.32 | 87.24 | 68.61 |
| Frost | 100.00 | 64.12 | 57.09 | 50.75 | 146.53 | 75.52 | 27.19 | 42.05 | 36.58 | 30.79 | 47.77 | 40.72 | 38.63 |
| Gaussian Blur | 100.00 | 86.69 | 84.58 | 77.75 | 107.84 | 82.50 | 55.22 | 88.91 | 77.05 | 77.21 | 90.59 | 81.36 | 85.37 |
| Gaussian Noise | 100.00 | 52.01 | 51.36 | 56.02 | 130.74 | 66.75 | 30.16 | 56.81 | 38.29 | 52.62 | 73.31 | 59.86 | 54.49 |
| Glass Blur | 100.00 | 89.71 | 85.46 | 81.43 | 98.30 | 84.73 | 66.52 | 93.59 | 86.00 | 87.28 | 96.53 | 86.27 | 90.24 |
| Impulse Noise | 100.00 | 47.18 | 44.71 | 45.78 | 122.95 | 61.19 | 28.27 | 44.55 | 31.93 | 39.72 | 63.83 | 48.63 | 48.68 |
| JPEG Compression | 100.00 | 69.79 | 59.62 | 60.96 | 131.33 | 78.90 | 43.49 | 82.29 | 65.82 | 63.30 | 144.27 | 88.13 | 108.22 |
| Motion Blur | 100.00 | 65.05 | 56.10 | 51.42 | 106.50 | 58.86 | 33.26 | 65.84 | 54.55 | 54.13 | 80.88 | 50.12 | 62.42 |
| Pixelate | 100.00 | 82.35 | 71.52 | 66.00 | 52.11 | 27.31 | 15.88 | 80.34 | 66.30 | 65.02 | 109.24 | 100.70 | 101.51 |
| Saturate | 100.00 | 63.44 | 53.74 | 47.61 | 250.68 | 116.28 | 48.06 | 57.26 | 47.97 | 47.07 | 75.29 | 62.40 | 58.34 |
| Shot Noise | 100.00 | 52.69 | 51.85 | 56.73 | 128.00 | 66.02 | 30.12 | 56.20 | 38.75 | 51.72 | 73.51 | 62.09 | 57.99 |
| Snow | 100.00 | 54.55 | 48.57 | 43.18 | 134.88 | 61.12 | 26.04 | 54.29 | 46.02 | 42.14 | 57.70 | 39.38 | 47.00 |
| Spatter | 100.00 | 39.86 | 32.09 | 29.41 | 117.51 | 48.16 | 21.03 | 33.10 | 28.59 | 24.33 | 32.71 | 23.79 | 22.92 |
| Speckle Noise | 100.00 | 44.78 | 40.91 | 34.08 | 132.49 | 60.64 | 26.89 | 42.92 | 30.43 | 34.07 | 61.92 | 48.85 | 48.80 |
| Zoom Blur | 100.00 | 82.47 | 68.22 | 64.74 | 125.18 | 84.89 | 52.90 | 82.72 | 70.04 | 70.37 | 93.27 | 77.34 | 77.96 |
| mCE | 100.00 | 67.55 | 59.52 | 56.92 | 153.7 | 79.28 | 42.26 | 65.05 | 53.08 | 53.76 | 77.86 | 63.04 | 64.98 |

Salient and Non-Salient Patch Drop: We evaluate the robustness of VSSMs against salient (foreground) and non-salient (background) patch drop. Using a self-supervised ViT model, DINO [3], we effectively segment salient objects by exploiting the spatial positions of information flowing into the final feature vector within the last attention block. This allows us to control the amount of salient information captured within the selected patches by thresholding. Similarly, we also select the least salient regions of the image and drop the patches containing the lowest foreground information [37]. Similar to [37], the patch size is fixed to 16×16 for this experiment. Tab. 2 (top) shows that *VSSM models demonstrate notable robustness when foreground content is removed, outperforming both convolutional (ResNet and ConvNeXt) and the ViT transformer family. Their performance is on par with the Swin family until a 50% salient patch drop, beyond which Swin transformers exhibit better robustness*, maintaining higher accuracy compared to VSSMs. The trend for non-salient patch drops is similar and is shown in the Appendix B.2.

Patch Shuffling: VSSMs process images as a sequence of patches, and the order of these patches represents the overall image structure and global composition. To evaluate the robustness of VSSMs to patch permutations, we define a shuffling operation on the input image patches, which destroys the image structure by changing the order of the patch sequence. Based on the dimensions of the patch size, we split the image into either 4, 8, 16, 32, 64 and 256 patches, which is then followed by random shuffling of the patches to evaluate the performance of models on spatial rearrangement of information. In Tab. 2 (bottom), we observe that VSSM family overall performs better than other models when the spatial structure of the input image is disturbed. *VSSM models generally demonstrate greater resilience to spatial structure disturbances than Swin models.*

Table 4: Top-1 classification accuracy for the domain generalization setting across various architectures and datasets. Models trained on ImageNet are evaluated on datasets with domain shifts.

| Model ↓ | ImageNet | ImageNetV2 | ImageNet-S | ImageNet-A | ImageNet-R | Average |
|------------|----------|---------------------------|---------------------------|---------------------------|---------------------------|---------------------------|
| ConvNext-T | 81.87 | 70.67 _(-11.20) | 33.96 _(-47.91) | 10.48 _(-71.39) | 32.53 _(-49.34) | 36.90 _(-44.97) |
| ViT-T | 75.35 | 63.05 _(-12.30) | 20.88 _(-54.47) | 3.31 _(-72.04) | 20.29 _(-55.06) | 26.88 _(-48.47) |
| Swin-T | 80.91 | 69.31 _(-11.60) | 29.24 _(-51.67) | 8.93 _(-71.98) | 28.52 _(-52.39) | 34.00 _(-46.91) |
| VSSM-T | 82.28 | 71.16 _(-11.12) | 33.99 _(-48.29) | 12.08 _(-70.20) | 32.05 _(-50.23) | 37.32 _(-44.96) |
| ConvNext-S | 82.82 | 72.07 _(-10.75) | 37.16 _(-45.66) | 14.43 _(-68.39) | 35.57 _(-47.25) | 39.81 _(-43.01) |
| ViT-S | 81.40 | 69.98 _(-11.42) | 32.77 _(-48.63) | 13.09 _(-68.31) | 31.14 _(-50.26) | 36.74 _(-44.66) |
| Swin-S | 82.90 | 71.62 _(-11.28) | 31.97 _(-50.93) | 15.72 _(-67.18) | 31.93 _(-50.97) | 37.81 _(-45.09) |
| VSSM-S | 83.48 | 73.01 _(-10.47) | 36.98 _(-46.50) | 16.45 _(-67.03) | 35.75 _(-47.73) | 40.55 _(-42.93) |
| ConvNext-B | 83.75 | 73.68 _(-10.07) | 38.23 _(-45.52) | 18.16 _(-65.59) | 36.66 _(-47.09) | 41.68 _(-42.07) |
| ViT-B | 84.40 | 73.84 _(-10.56) | 43.01 _(-41.39) | 24.09 _(-60.31) | 41.03 _(-43.37) | 45.49 _(-38.91) |
| Swin-B | 83.08 | 72.09 _(-10.99) | 32.62 _(-50.46) | 17.95 _(-65.13) | 33.23 _(-49.85) | 38.97 _(-44.11) |
| VSSM-B | 83.76 | 73.22 _(-10.54) | 38.53 _(-45.23) | 18.35 _(-65.41) | 35.99 _(-47.77) | 41.52 _(-42.24) |

Table 5: Top-1 classification accuracy of various architectures on the ImageNet-E dataset [26] (left) and ImageNet-B dataset [34] (right).

| Dataset → | ImageNet-E | | | | | | | | | ImageNet-B | | | | |
|------------|-----------------|----------------|----------------------------|-----------|-------|-------|-------|-------------|----------|------------|---------|-------|-------|---------|
| Model ↓ | $\lambda = -20$ | $\lambda = 20$ | $\lambda = 20(\text{adv})$ | Random-BG | 0.1 | 0.08 | 0.05 | Random Pos. | Original | Original | Caption | Class | Color | Texture |
| ResNet-50 | 88.74 | 86.76 | 73.02 | 84.05 | 89.19 | 86.60 | 77.34 | 73.30 | 94.55 | 98.60 | 94.00 | 96.60 | 88.20 | 85.70 |
| ConvNext-T | 90.95 | 90.03 | 76.88 | 88.09 | 93.01 | 90.87 | 83.09 | 80.19 | 96.09 | 98.20 | 93.20 | 95.10 | 88.80 | 87.40 |
| ConvNext-S | 91.96 | 90.76 | 78.52 | 88.99 | 93.61 | 91.66 | 85.34 | 82.19 | 96.07 | 98.80 | 94.00 | 96.70 | 90.70 | 89.60 |
| ConvNext-B | 92.30 | 91.52 | 80.44 | 90.00 | 93.91 | 93.01 | 86.65 | 83.75 | 96.41 | 99.20 | 93.60 | 96.40 | 90.60 | 91.40 |
| ViT-T | 80.81 | 77.07 | 46.78 | 69.07 | 81.06 | 76.55 | 64.13 | 57.86 | 91.08 | 95.20 | 85.50 | 90.40 | 67.30 | 64.50 |
| ViT-S | 86.77 | 83.46 | 63.19 | 80.58 | 87.98 | 84.05 | 74.29 | 69.94 | 94.74 | 97.70 | 89.20 | 94.30 | 84.20 | 80.60 |
| ViT-B | 90.07 | 87.48 | 71.28 | 84.88 | 91.01 | 88.64 | 79.99 | 76.42 | 95.66 | 98.00 | 90.40 | 93.80 | 86.20 | 84.80 |
| VSSM-T | 91.15 | 89.87 | 75.18 | 87.41 | 92.09 | 91.06 | 83.66 | 79.71 | 95.84 | 98.50 | 92.20 | 96.30 | 87.20 | 86.80 |
| VSSM-S | 92.03 | 90.79 | 76.15 | 88.81 | 93.22 | 92.25 | 85.57 | 81.89 | 96.37 | 99.20 | 94.10 | 97.40 | 90.90 | 89.50 |
| VSSM-B | 92.37 | 91.27 | 77.30 | 89.11 | 93.70 | 92.64 | 86.03 | 83.62 | 96.37 | 99.10 | 94.00 | 96.50 | 90.80 | 89.80 |
| Swin-T | 90.05 | 88.83 | 71.51 | 86.19 | 91.08 | 88.94 | 79.39 | 76.49 | 95.27 | 97.90 | 91.70 | 95.30 | 85.50 | 84.00 |
| Swin-S | 90.67 | 88.86 | 73.35 | 87.25 | 91.91 | 89.68 | 81.55 | 78.81 | 96.25 | 98.30 | 91.80 | 95.50 | 86.10 | 85.40 |
| Swin-B | 91.08 | 89.96 | 75.09 | 87.87 | 92.62 | 91.22 | 83.43 | 80.65 | 95.95 | 98.60 | 92.30 | 95.60 | 89.20 | 86.70 |

3.1.2 Robustness against ImageNet Corruptions

To evaluate the robustness of VSSMs in real-world scenarios, we performed experiments on several corrupted versions of the ImageNet dataset, which can be grouped into two categories based on the type of changes they introduce to the images. The **first category** includes datasets that make overall global compositional changes, such as *ImageNet-C* [17], which evaluates robustness against 19 common distortions across five categories (noise, blur, weather, and digital-based corruptions) with varying severity levels. Additionally, datasets like *ImageNetV2* [41], *ImageNet-A* [19], *ImageNet-R* [18], and *ImageNet-S* [11] also fall into this category, as they introduce domain shifts that affect the global composition of the images. For details of these datasets, see Appendix B.5. The **second category** consists of datasets that provide more control in editing the images and focus on fine-grained details. *ImageNet-E* [26] assesses classifiers’ robustness to changes in background, object size, position, and direction, while *ImageNet-B* [34] introduces diverse object-to-background changes using text-to-image, image-to-text, and image-to-segment models, preserving original object semantics while varying backgrounds to include both natural and adversarial changes. These datasets use diffusion models to generate various object-to-background compositional changes to test the resilience of models.

Robustness against Global Corruptions: The performance of various models on ImageNet-C is reported in terms of the mean corruption error (mCE) in Tab. 3. The mCE (*lower is better*) represents the average error of the model across various common corruptions at multiple intensity levels, normalized by the ResNet-50’s standard accuracy. VSSM-T has the lowest mCE among all the ‘T’ versions, followed by VSSM-S, which performs significantly better than its ‘S’ counterparts. However, among the ‘B’ family, ViT-B achieves the lowest mCE score, possibly due to its pretraining on ImageNet21k and finetuning on ImageNet 1k. Notably, the mCE error of all Base models (VSSM, Swin, ConvNext) is larger than their Small counterparts, indicating that robust performance may not uniformly improve with model size. Similarly, the top-1 classification accuracy on domain-shifted datasets, including ImageNetV2 [41], ImageNet-A [19], ImageNet-R [18], and ImageNet-S [11] is

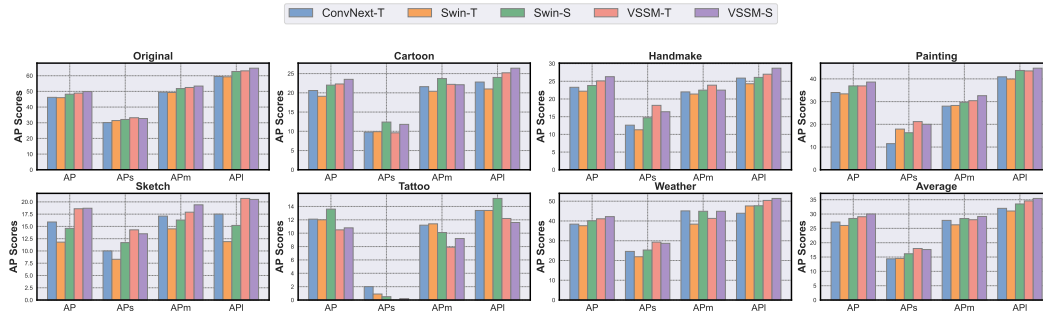


Figure 2: Average Precision (AP) scores for different architectures on the COCO-O dataset [8], detailing results for small (APs), medium (APm), and large objects (API).

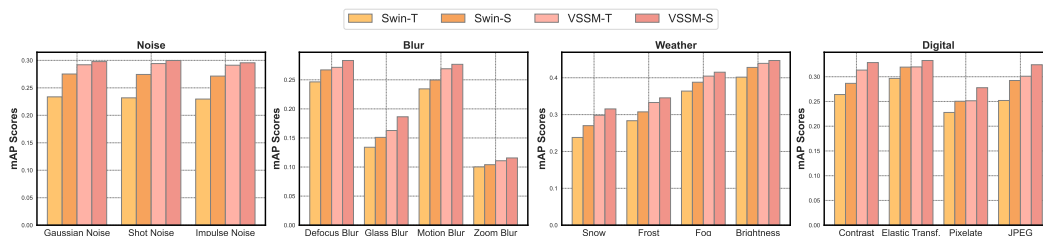


Figure 3: Mean Average Precision (mAP) score for different architectures on COCO-C dataset.

shown in Tab. 4. *VSSM-T and VSSM-S have the least average performance drop compared to their Swin and ConvNext-based counterparts.* For Base models, ViT performs the best, which may be attributed to its pretraining on the larger ImageNet21k dataset.

Robustness against Fine-grained Corruptions: Tab. 5 (left) shows the robustness of models on ImageNet-E against variations in background complexity, object size, and object positioning. Lower λ values correspond to low background texture complexity, whereas higher λ values indicate high background texture complexity, with $\lambda = 20$ (adv) representing the extreme case of adversarially optimized high texture complexity. The object in the scene is resized proportionally to its original size, specifically to (0.1, 0.08, 0.05), and is placed at random locations within the scene. As can be observed from the results, VSSM models show higher resilience to background changes compared to the corresponding Swin and ViT transformer families, with performance comparable to the advanced ConvNeXt models. As background complexity increases or object size decreases, the performance of all models declines, but the drop is less significant for the VSSM and ConvNeXt models compared to the Transformer-based models, demonstrating their robustness to object size variations. Similar trends are observed for the ImageNet-B dataset in Tab. 5 (right). This dataset introduces background changes in the images by using a diffusion model to modify the background with textual guidance, such as class or caption information as prompts, or by adding color and texture prompts. *The VSSM family demonstrates superior performance compared to all Transformer-based variants and maintains performance better or comparable to the advanced ConvNext models.* For further analysis across other model families, refer to Appendix B.5.

3.1.3 Robustness Evaluation for Object Detection

To evaluate the robustness of VSSMs, transformers, and CNNs for object detection, we use COCO-O [8], COCO-DC [34], and COCO-C datasets. COCO-O contains 6,782 images and 26,624 labeled bounding boxes across six challenging domains: sketch, cartoon, painting, weather, handmake, and tattoo. COCO-DC is a subset of 1,127 images from the COCO 2017 validation set with diverse background changes introduced by a diffusion model. COCO-C comprises the COCO-2017 evaluation set, corrupted with common ImageNet-C style corruptions at various intensity levels. We assess performance using Average Precision (AP) and AP by object sizes (APs, APm, API) on five models: ConvNext-T, Swin-T, Swin-S, VSSM-T, and VSSM-S.

Table 6: Average Precision (AP) scores for different architectures on the COCO-DC dataset [34], detailing results for small (APs), medium (APm), and large objects (API).

| Model | AP | APs | APm | API | AP | APs | APm | API | AP | APs | APm | API | AP | APs | APm | API |
|------------|----------|------|------|------|-------|------|------|------|---------|------|------|------|----------------|----------------|----------------|----------------|
| | Original | | | | Color | | | | Texture | | | | Average | | | |
| ConvNext-T | 66.2 | 41.0 | 61.3 | 71.4 | 55.0 | 26.3 | 49.0 | 60.6 | 53.5 | 26.5 | 47.5 | 60.5 | 54.25 (-11.95) | 26.40 (-14.60) | 48.25 (-13.05) | 60.55 (-10.85) |
| Swin-T | 66.3 | 45.1 | 61.6 | 71.6 | 55.1 | 29.2 | 48.0 | 62.0 | 53.6 | 31.4 | 45.2 | 61.4 | 54.35 (-11.95) | 30.30 (-14.80) | 46.60 (-15.00) | 61.70 (-09.90) |
| Swin-S | 69.1 | 43.7 | 62.3 | 75.9 | 57.4 | 30.1 | 49.1 | 64.3 | 56.0 | 26.8 | 45.4 | 64.3 | 56.70 (-12.40) | 28.45 (-15.25) | 47.25 (-15.05) | 64.30 (-11.60) |
| VSSM-T | 69.3 | 47.1 | 64.4 | 75.5 | 56.2 | 30.9 | 48.4 | 63.7 | 53.2 | 29.2 | 44.9 | 61.0 | 54.57 (-14.73) | 30.05 (-17.05) | 46.65 (-17.75) | 62.35 (-13.15) |
| VSSM-S | 70.9 | 51.7 | 64.6 | 77.1 | 56.7 | 31.3 | 48.9 | 64.3 | 55.7 | 26.8 | 47.4 | 64.4 | 56.20 (-14.70) | 29.05 (-22.65) | 48.15 (-16.45) | 64.35 (-12.75) |

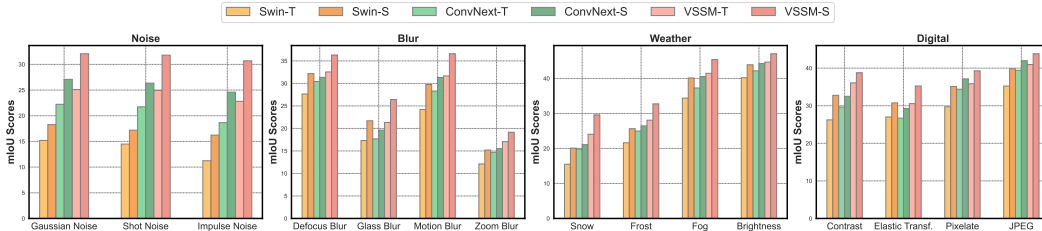


Figure 4: Mean Intersection over Union (mIoU) score for different architectures on AED20k-C dataset.

Fig. 2 shows that the VSSM-S and VSSM-T models consistently outperform other architectures in most COCO-O scenarios, achieving the highest AP scores in the original validation set and maintaining their lead in out-of-distribution domains like cartoon, painting, sketch, and weather. However, the tattoo domain is challenging for all models, with VSSMs exhibiting lower AP and APm compared to the Swin and ConvNext models. On average, VSSM-S and VSSM-T achieve AP scores of 42.2% and 41.1%, surpassing the Swin and ConvNext models. Similarly, Fig. 3 shows that VSSM-T and VSSM-S generally outperform their Swin counterparts across various common corruptions in object detection, indicating their superior robustness. Even the smallest VSSM-T surpasses the larger Swin-S in most corruption scenarios, demonstrating VSSMs’ effectiveness in maintaining high accuracy under common corruptions. Both model families exhibit noticeable performance drops when dealing with ‘Glass Blur’ and ‘Zoom Blur’ corruptions. However, On COCO-DC (Tab. 6), the high performance of VSSM models on clean images does not transfer well to maintain their lead in color and texture background variations of the images. Swin-S model achieves the highest average AP score of 56.70 across the background variations, followed by score of 56.20 by VSSM-S model.

3.1.4 Robustness Evaluation for Semantic Segmentation

To assess the robustness of segmentation models, we employ the ADE20K dataset [48]. We corrupt 2,000 images from the ADE20K validation set using ImageNet-C [17] corruptions at various intensity levels. The performance of the models is evaluated using the mean Intersection over Union (mIoU).

We observe a similar trend in the performance of segmentation models on the corrupted ADE20K dataset as seen with object detection models on COCO-C. Fig. 4 shows that VSSM-T and VSSM-S consistently outperform their Swin counterparts across various ImageNet-C corruptions in object segmentation, demonstrating superior robustness. The high performance of VSSM models on the original dataset also transfers effectively to the corrupted version of the dataset. Notably, even the smallest VSSM-T model surpasses the larger Swin-S model in most of the corruption scenarios.

3.2 Robustness against Adversarial Attacks

In this section, we evaluate the robustness of VSSMs against spatial and frequency-based adversarial attacks. We also compare the performance of adversarially fine-tuned VSSM models on CIFAR-10 [22] and Imagenette [1] downstream dataset with ViT and Swin models.

Adversarial Attacks in Spatial Domain: We conduct experiments in both white-box and black-box settings using the Fast Gradient Sign Method (FGSM) [13] and Projected Gradient Descent (PGD) [32] with an l_∞ -norm and $\epsilon = 8/255$. FGSM is a single-step process, while PGD operates as a multistep method, iterating for 20 steps with a step size of $2/255$. Tab. 7 (top) displays the robust accuracy scores under white-box (diagonal entries) and black-box (off-diagonal entries) adversarial attacks for FGSM. *VSSM-T and VSSM-S exhibit higher white-box attack robustness compared to*

Table 7: Robust accuracy of models under white-box and black-box settings for FGSM and PGD attacks. Adversarial examples crafted on surrogate models are used to evaluate robustness of target models.

| Target → | VSSM-T | VSSM-S | VSSM-B | ResNet-50 | ConvNext-T | ConvNext-S | ConvNext-B | ViT-T | ViT-S | ViT-B | Swin-T | Swin-S | Swin-B |
|-------------|--|--------|--------|-----------|------------|------------|------------|-------|-------|-------|--------|--------|--------|
| Surrogate ↓ | Fast Gradient Sign Method (FGSM) at $\epsilon = \frac{8}{255}$ | | | | | | | | | | | | |
| VSSM-T | 42.90 | 66.34 | 65.10 | 80.20 | 72.66 | 73.80 | 72.84 | 79.46 | 83.64 | 86.94 | 72.22 | 76.38 | 74.60 |
| VSSM-S | 62.24 | 48.42 | 63.00 | 79.70 | 71.40 | 71.04 | 70.18 | 78.42 | 81.56 | 84.58 | 70.96 | 72.92 | 71.14 |
| VSSM-B | 65.52 | 66.96 | 51.24 | 81.22 | 73.54 | 73.20 | 72.32 | 79.12 | 83.62 | 86.24 | 73.24 | 76.30 | 73.88 |
| ResNet-50 | 81.38 | 83.24 | 83.84 | 30.46 | 80.30 | 82.20 | 83.38 | 75.94 | 84.74 | 89.12 | 80.64 | 85.00 | 85.42 |
| ConvNext-T | 69.00 | 71.46 | 71.18 | 77.96 | 36.36 | 61.96 | 63.76 | 76.92 | 82.74 | 85.58 | 67.06 | 71.88 | 70.78 |
| ConvNext-S | 69.54 | 70.62 | 70.48 | 79.48 | 63.48 | 49.10 | 63.62 | 78.48 | 82.94 | 85.02 | 69.24 | 71.54 | 69.74 |
| ConvNext-B | 70.54 | 71.78 | 69.78 | 81.72 | 67.34 | 66.24 | 51.32 | 80.26 | 83.98 | 86.22 | 69.86 | 73.44 | 70.84 |
| ViT-T | 85.92 | 88.30 | 88.88 | 82.68 | 85.08 | 86.56 | 88.06 | 2.28 | 50.04 | 69.90 | 75.66 | 79.72 | 82.32 |
| ViT-S | 81.74 | 83.76 | 84.46 | 81.70 | 82.34 | 82.78 | 84.38 | 45.40 | 11.02 | 54.82 | 72.50 | 75.98 | 77.88 |
| ViT-B | 82.46 | 84.02 | 84.48 | 81.90 | 82.04 | 82.24 | 83.62 | 58.50 | 53.84 | 24.24 | 75.82 | 77.62 | 78.54 |
| Swin-T | 72.40 | 76.06 | 75.58 | 82.82 | 71.46 | 72.12 | 71.96 | 76.48 | 80.66 | 85.46 | 28.86 | 56.22 | 55.12 |
| Swin-S | 78.24 | 79.10 | 79.30 | 85.46 | 77.96 | 77.10 | 77.02 | 79.38 | 83.04 | 86.58 | 61.94 | 48.00 | 63.90 |
| Swin-B | 78.88 | 79.40 | 79.04 | 86.60 | 78.16 | 78.46 | 77.32 | 81.48 | 84.74 | 87.64 | 66.82 | 68.28 | 54.76 |
| | Projected Gradient Decent (PGD) at $\epsilon = \frac{8}{255}$ | | | | | | | | | | | | |
| VSSM-T | 0.00 | 37.26 | 35.56 | 81.44 | 63.54 | 67.18 | 65.88 | 82.58 | 89.16 | 91.80 | 65.76 | 74.72 | 71.50 |
| VSSM-S | 16.88 | 0.02 | 23.94 | 77.54 | 56.24 | 57.72 | 56.16 | 79.26 | 86.06 | 89.42 | 58.92 | 65.92 | 61.46 |
| VSSM-B | 15.98 | 25.26 | 0.00 | 77.38 | 56.30 | 57.94 | 53.42 | 79.76 | 86.24 | 89.94 | 57.40 | 66.52 | 61.74 |
| ResNet-50 | 83.34 | 86.98 | 87.04 | 0.00 | 81.00 | 84.92 | 86.30 | 82.48 | 89.96 | 93.18 | 84.18 | 89.24 | 89.12 |
| ConvNext-T | 60.58 | 67.06 | 66.48 | 79.76 | 0.00 | 31.32 | 39.70 | 80.44 | 87.28 | 90.46 | 56.02 | 66.62 | 64.40 |
| ConvNext-S | 58.04 | 63.20 | 62.96 | 78.22 | 24.96 | 0.00 | 33.96 | 80.02 | 86.20 | 89.86 | 52.70 | 62.58 | 60.54 |
| ConvNext-B | 58.24 | 64.04 | 60.40 | 80.80 | 35.84 | 36.60 | 0.00 | 81.48 | 87.22 | 90.36 | 51.80 | 63.16 | 58.62 |
| ViT-T | 92.10 | 93.82 | 94.26 | 88.14 | 90.44 | 92.18 | 93.28 | 0.00 | 55.58 | 77.34 | 84.52 | 88.16 | 89.24 |
| ViT-S | 87.28 | 89.34 | 89.70 | 85.96 | 86.34 | 87.90 | 89.26 | 38.16 | 0.00 | 48.68 | 76.98 | 80.34 | 82.48 |
| ViT-B | 86.18 | 87.74 | 87.72 | 85.04 | 85.56 | 86.10 | 87.62 | 53.50 | 37.48 | 0.00 | 77.02 | 79.56 | 80.86 |
| Swin-T | 83.10 | 87.58 | 87.06 | 89.58 | 79.30 | 81.52 | 80.28 | 83.32 | 89.82 | 92.80 | 0.00 | 39.00 | 37.88 |
| Swin-S | 83.08 | 86.28 | 86.26 | 89.76 | 79.60 | 80.68 | 79.84 | 82.96 | 88.80 | 92.38 | 25.40 | 0.00 | 31.44 |
| Swin-B | 82.52 | 85.12 | 84.78 | 89.88 | 79.18 | 80.08 | 78.92 | 84.24 | 89.74 | 92.86 | 27.30 | 34.36 | 0.02 |

Table 8: Robust accuracy of various architectures against low-frequency and high-frequency-based perturbation using PGD attack at varying level of perturbation budget $\epsilon \in \{1/255, 2/255, 4/255, 8/255, 12/255, 16/255\}$.

| Filter → | Low-Pass | | | | | | High-Pass | | | | | | All-Pass | | |
|------------------------|----------|-------|-------|-------|--------|--------|-----------|-------|-------|-------|--------|--------|----------|-------|-------|
| $\epsilon \rightarrow$ | 1/255 | 2/255 | 4/255 | 8/255 | 12/255 | 16/255 | 1/255 | 2/255 | 4/255 | 8/255 | 12/255 | 16/255 | 1/255 | 2/255 | 4/255 |
| ResNet-50 | 94.94 | 93.28 | 91.38 | 88.42 | 87.74 | 87.86 | 72.68 | 43.58 | 28.70 | 16.38 | 11.62 | 10.76 | 29.68 | 2.04 | 0.08 |
| ConvNext-T | 95.98 | 95.46 | 94.60 | 91.76 | 89.70 | 89.50 | 58.26 | 26.46 | 13.62 | 4.40 | 2.38 | 2.06 | 20.18 | 1.60 | 0.02 |
| ConvNext-S | 96.52 | 96.14 | 95.80 | 93.48 | 91.70 | 91.36 | 66.58 | 34.66 | 20.50 | 7.38 | 3.66 | 3.12 | 30.10 | 3.98 | 0.08 |
| ConvNext-B | 96.84 | 96.76 | 96.14 | 93.62 | 92.40 | 91.72 | 64.96 | 39.26 | 22.98 | 8.76 | 5.46 | 4.56 | 31.02 | 6.24 | 0.18 |
| ViT-T | 85.52 | 77.56 | 68.50 | 53.02 | 47.28 | 46.32 | 69.32 | 38.48 | 19.24 | 5.52 | 2.56 | 1.88 | 11.14 | 0.16 | 0.00 |
| ViT-S | 93.12 | 88.60 | 83.50 | 72.84 | 69.22 | 69.06 | 77.14 | 46.48 | 27.94 | 11.08 | 6.76 | 5.28 | 18.74 | 0.42 | 0.00 |
| ViT-B | 94.66 | 90.28 | 87.40 | 80.68 | 77.50 | 77.26 | 85.74 | 61.84 | 46.52 | 26.18 | 18.28 | 16.28 | 30.94 | 1.30 | 0.08 |
| VSSM-T | 96.46 | 96.04 | 95.22 | 93.02 | 91.70 | 91.18 | 58.12 | 32.50 | 16.46 | 5.74 | 2.92 | 2.82 | 24.00 | 5.16 | 0.28 |
| VSSM-S | 97.02 | 96.90 | 96.48 | 94.10 | 92.62 | 92.24 | 67.64 | 44.00 | 28.18 | 11.36 | 6.46 | 5.48 | 32.54 | 10.90 | 0.84 |
| VSSM-B | 97.28 | 97.00 | 96.56 | 94.28 | 92.90 | 92.24 | 66.60 | 45.44 | 27.68 | 10.36 | 6.08 | 4.78 | 33.10 | 9.88 | 0.40 |
| Swin-T | 96.24 | 95.86 | 95.24 | 93.28 | 91.94 | 91.30 | 49.12 | 23.42 | 9.78 | 2.06 | 1.10 | 0.88 | 12.60 | 1.86 | 0.00 |
| Swin-S | 96.92 | 96.60 | 96.16 | 94.26 | 93.30 | 92.70 | 60.70 | 36.50 | 20.18 | 7.48 | 3.90 | 3.30 | 25.92 | 6.74 | 0.42 |
| Swin-B | 96.82 | 96.94 | 96.24 | 94.72 | 94.10 | 93.34 | 61.04 | 40.50 | 24.68 | 9.30 | 5.82 | 4.34 | 30.14 | 9.76 | 0.70 |

their Swin Transformer counterparts, but this pattern does not extend to the larger VSSM-B model. This indicates that VSSM’s robustness advantage over Swin Transformers may not consistently scale with increased model size. For black-box settings, generally attacks transfer more easily within the same architecture family (e.g., from VSSM-T to VSSM-S) than across different architectures (e.g., from VSSM to Swin Transformer). With stronger PGD-20 attack (Tab. 7 (bottom)), we observe all the models performance drops to zero under white-box setting, revealing their vulnerability to stronger adversarial attacks. Transferability in black-box setting for PGD attack shows similar trend to that obtained for FGSM attack. For further analysis across other model families, refer to Appendix A.

Adversarial Attacks in the Frequency Domain: We evaluate the robustness of VSSMs against frequency-specific adversarial attacks crafted using Projected Gradient Descent (PGD). These perturbations are constrained to designated frequency bands through a discrete cosine transform (DCT) mask filter [33]. *Results in Tab. 8 (left) demonstrate that all VSSM models maintain robustness above 90% for low-frequency perturbations up to $\epsilon = 16$, indicating strong resilience similar to the ConvNext and Swin transformer counterparts.* ViT models exhibit the most performance drop under low-frequency adversarial attacks. For high-frequency adversarial attacks (Tab. 8 (middle)), the robustness of all models decreases more rapidly with increasing perturbation strength, although ViT-based models show the highest robustness. Finally, for standard attacks where the complete

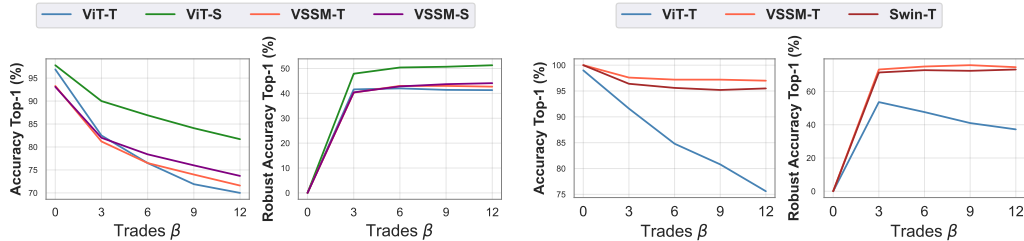


Figure 5: Clean and Robust accuracy of models evaluated on CIFAR-10 (*left*) and Imagenette (*right*).

frequency range is used to generate adversarial examples, VSSM models display higher robustness compared to other models, including ConvNext, ViT, and Swin.

Adversarial Fine-tuning on Downstream Datasets: We adversarially fine-tune ImageNet pre-trained VSSM, ViT, and Swin on downstream datasets using the TRADES [47] objective with varying robustness strength β and an l_∞ perturbation budget $\epsilon = 8$. In Fig. 5, we plot the clean and robust accuracy under PGD-100 at $\epsilon = 8$. On Imagenette [1], VSSM-T shows strong performance in both clean and robust accuracy across different β levels, followed closely by Swin-T, while ViT-T exhibits the lowest robustness. However, on the low-resolution CIFAR-10 dataset with significantly lower number of patches, attention-based ViT models perform better than Mamba-based VSSM models.

4 Conclusion

In conclusion, we present a comprehensive evaluation of the robustness of Vision State-Space Models (VSSMs) under diverse natural and adversarial perturbations, highlighting both their strengths and weaknesses compared to transformers and CNNs. Through rigorous experiments, we demonstrated the capabilities and limitations of VSSMs classifiers in handling occlusions, common corruptions, and adversarial attacks, as well as their resilience to object-background compositional changes in complex visual scenes. Additionally, we show that VSSM-based models are generally more robust to real-world corruptions in the dense prediction tasks, including detection and segmentation. As an early work in this area, our findings significantly enhance the understanding of VSSMs’ robustness and set the stage for future research aimed at improving the reliability and effectiveness of visual perception systems in real-world scenarios.

References

- [1] Imagenette. <https://github.com/fastai/imagenette/>. Accessed: 2024-05-10.
- [2] Yutong Bai, Jieru Mei, Alan L Yuille, and Cihang Xie. Are transformers more robust than cnns? *Advances in neural information processing systems*, 34:26831–26843, 2021.
- [3] Mathilde Caron, Hugo Touvron, Ishan Misra, Hervé Jégou, Julien Mairal, Piotr Bojanowski, and Armand Joulin. Emerging properties in self-supervised vision transformers. In *Proceedings of the IEEE/CVF international conference on computer vision*, pages 9650–9660, 2021.
- [4] Guo Chen, Yifei Huang, Jilan Xu, Baoqi Pei, Zhe Chen, Zhiqi Li, Jiahao Wang, Kunchang Li, Tong Lu, and Limin Wang. Video mamba suite: State space model as a versatile alternative for video understanding. *arXiv preprint arXiv:2403.09626*, 2024.
- [5] Kai Chen, Jiaqi Wang, Jiangmiao Pang, Yuhang Cao, Yu Xiong, Xiaoxiao Li, Shuyang Sun, Wansen Feng, Ziwei Liu, Jiarui Xu, et al. Mmdetection: Open mmlab detection toolbox and benchmark. *arXiv preprint arXiv:1906.07155*, 2019.
- [6] Keyan Chen, Bowen Chen, Chenyang Liu, Wenyuan Li, Zhengxia Zou, and Zhenwei Shi. Rsmamba: Remote sensing image classification with state space model. *arXiv preprint arXiv:2403.19654*, 2024.
- [7] MMSegmentation Contributors. Mmsegmentation: Openmmlab semantic segmentation toolbox and benchmark, 2020.

- [8] Edoardo DeBenedetti, Vikash Sehwal, and Prateek Mittal. A light recipe to train robust vision transformers. In *2023 IEEE Conference on Secure and Trustworthy Machine Learning (SaTML)*, pages 225–253. IEEE, 2023.
- [9] Alexey Dosovitskiy, Lucas Beyer, Alexander Kolesnikov, Dirk Weissenborn, Xiaohua Zhai, Thomas Unterthiner, Mostafa Dehghani, Matthias Minderer, Georg Heigold, Sylvain Gelly, et al. An image is worth 16x16 words: Transformers for image recognition at scale. *arXiv preprint arXiv:2010.11929*, 2020.
- [10] Nathan Drenkow, Numair Sani, Ilya Shpitser, and Mathias Unberath. A systematic review of robustness in deep learning for computer vision: Mind the gap? *arXiv preprint arXiv:2112.00639*, 2021.
- [11] Shanghua Gao, Zhong-Yu Li, Ming-Hsuan Yang, Ming-Ming Cheng, Junwei Han, and Philip Torr. Large-scale unsupervised semantic segmentation. *IEEE transactions on pattern analysis and machine intelligence*, 2022.
- [12] Robert Geirhos, Patricia Rubisch, Claudio Michaelis, Matthias Bethge, Felix A Wichmann, and Wieland Brendel. Imagenet-trained cnns are biased towards texture; increasing shape bias improves accuracy and robustness. *arXiv preprint arXiv:1811.12231*, 2018.
- [13] Ian J Goodfellow, Jonathon Shlens, and Christian Szegedy. Explaining and harnessing adversarial examples. *arXiv preprint arXiv:1412.6572*, 2014.
- [14] Albert Gu and Tri Dao. Mamba: Linear-time sequence modeling with selective state spaces. *arXiv preprint arXiv:2312.00752*, 2023.
- [15] Albert Gu, Karan Goel, and Christopher Ré. Efficiently modeling long sequences with structured state spaces. *arXiv preprint arXiv:2111.00396*, 2021.
- [16] Kaiming He, Georgia Gkioxari, Piotr Dollár, and Ross Girshick. Mask r-cnn. In *Proceedings of the IEEE international conference on computer vision*, pages 2961–2969, 2017.
- [17] Dan Hendrycks and Thomas Dietterich. Benchmarking neural network robustness to common corruptions and perturbations. *arXiv preprint arXiv:1903.12261*, 2019.
- [18] Dan Hendrycks, Steven Basart, Norman Mu, Saurav Kadavath, Frank Wang, Evan Dorundo, Rahul Desai, Tyler Zhu, Samyak Parajuli, Mike Guo, et al. The many faces of robustness: A critical analysis of out-of-distribution generalization. In *Proceedings of the IEEE/CVF international conference on computer vision*, pages 8340–8349, 2021.
- [19] Dan Hendrycks, Kevin Zhao, Steven Basart, Jacob Steinhardt, and Dawn Song. Natural adversarial examples. In *Proceedings of the IEEE/CVF conference on computer vision and pattern recognition*, pages 15262–15271, 2021.
- [20] Qiufan Ji, Lin Wang, Cong Shi, Shengshan Hu, Yingying Chen, and Lichao Sun. Benchmarking and analyzing robust point cloud recognition: Bag of tricks for defending adversarial examples. In *Proceedings of the IEEE/CVF International Conference on Computer Vision*, pages 4295–4304, 2023.
- [21] Christoph Kamann and Carsten Rother. Benchmarking the robustness of semantic segmentation models. In *Proceedings of the IEEE/CVF Conference on Computer Vision and Pattern Recognition*, pages 8828–8838, 2020.
- [22] Alex Krizhevsky. Learning multiple layers of features from tiny images. *University of Toronto*, 05 2012.
- [23] Alex Krizhevsky, Ilya Sutskever, and Geoffrey E Hinton. Imagenet classification with deep convolutional neural networks. *Advances in neural information processing systems*, 25, 2012.
- [24] Amandeep Kumar, Muzammal Naseer, Sanath Narayan, Rao Muhammad Anwer, Salman Khan, and Hisham Cholakkal. Multi-modal generation via cross-modal in-context learning. 2024. URL <https://api.semanticscholar.org/CorpusID:270067594>.
- [25] Kunchang Li, Xinhao Li, Yi Wang, Yanan He, Yali Wang, Limin Wang, and Yu Qiao. Videomamba: State space model for efficient video understanding. *arXiv preprint arXiv:2403.06977*, 2024.
- [26] Xiaodan Li, Yuefeng Chen, Yao Zhu, Shuhui Wang, Rong Zhang, and Hui Xue. Imagenet-e: Benchmarking neural network robustness via attribute editing. In *Proceedings of the IEEE/CVF Conference on Computer Vision and Pattern Recognition*, pages 20371–20381, 2023.
- [27] Xiao Liu, Chenxu Zhang, and Lei Zhang. Vision mamba: A comprehensive survey and taxonomy. *arXiv preprint arXiv:2405.04404*, 2024.

- [28] Yue Liu, Yunjie Tian, Yuzhong Zhao, Hongtian Yu, Lingxi Xie, Yaowei Wang, Qixiang Ye, and Yunfan Liu. Vmamba: Visual state space model. *arXiv preprint arXiv:2401.10166*, 2024.
- [29] Ze Liu, Yutong Lin, Yue Cao, Han Hu, Yixuan Wei, Zheng Zhang, Stephen Lin, and Baining Guo. Swin transformer: Hierarchical vision transformer using shifted windows. In *Proceedings of the IEEE/CVF international conference on computer vision*, pages 10012–10022, 2021.
- [30] Zhuang Liu, Hanzi Mao, Chao-Yuan Wu, Christoph Feichtenhofer, Trevor Darrell, and Saining Xie. A convnet for the 2020s. In *Proceedings of the IEEE/CVF conference on computer vision and pattern recognition*, pages 11976–11986, 2022.
- [31] Wenjie Luo, Yujia Li, Raquel Urtasun, and Richard Zemel. Understanding the effective receptive field in deep convolutional neural networks. *Advances in neural information processing systems*, 29, 2016.
- [32] Aleksander Madry, Aleksandar Makelov, Ludwig Schmidt, Dimitris Tsipras, and Adrian Vladu. Towards deep learning models resistant to adversarial attacks. *arXiv preprint arXiv:1706.06083*, 2017.
- [33] Shishira R Maiya, Max Ehrlich, Vatsal Agarwal, Ser-Nam Lim, Tom Goldstein, and Abhinav Shrivastava. A frequency perspective of adversarial robustness. *arXiv preprint arXiv:2111.00861*, 2021.
- [34] Hashmat Shadab Malik, Muhammad Huzaifa, Muzammal Naseer, Salman Khan, and Fahad Shahbaz Khan. Objectcompose: Evaluating resilience of vision-based models on object-to-background compositional changes. *arXiv preprint arXiv:2403.04701*, 2024.
- [35] Harsh Mehta, Ankit Gupta, Ashok Cutkosky, and Behnam Neyshabur. Long range language modeling via gated state spaces. *arXiv preprint arXiv:2206.13947*, 2022.
- [36] Claudio Michaelis, Benjamin Mitzkus, Robert Geirhos, Evgenia Rusak, Oliver Bringmann, Alexander S Ecker, Matthias Bethge, and Wieland Brendel. Benchmarking robustness in object detection: Autonomous driving when winter is coming. *arXiv preprint arXiv:1907.07484*, 2019.
- [37] Muhammad Muzammal Naseer, Kanchana Ranasinghe, Salman H Khan, Munawar Hayat, Fahad Shahbaz Khan, and Ming-Hsuan Yang. Intriguing properties of vision transformers. *Advances in Neural Information Processing Systems*, 34:23296–23308, 2021.
- [38] Muzammal Naseer, Kanchana Ranasinghe, Salman Khan, Fahad Shahbaz Khan, and Fatih Porikli. On improving adversarial transferability of vision transformers. *arXiv preprint arXiv:2106.04169*, 2021.
- [39] Sayak Paul and Pin-Yu Chen. Vision transformers are robust learners. In *Proceedings of the AAAI conference on Artificial Intelligence*, volume 36, pages 2071–2081, 2022.
- [40] Francesco Pinto, Philip HS Torr, and Puneet K. Dokania. An impartial take to the cnn vs transformer robustness contest. In *European Conference on Computer Vision*, pages 466–480. Springer, 2022.
- [41] Benjamin Recht, Rebecca Roelofs, Ludwig Schmidt, and Vaishaal Shankar. Do imagenet classifiers generalize to imagenet? In *International conference on machine learning*, pages 5389–5400. PMLR, 2019.
- [42] Jue Wang, Wentao Zhu, Pichao Wang, Xiang Yu, Linda Liu, Mohamed Omar, and Raffay Hamid. Selective structured state-spaces for long-form video understanding. In *Proceedings of the IEEE/CVF Conference on Computer Vision and Pattern Recognition*, pages 6387–6397, 2023.
- [43] Tete Xiao, Yingcheng Liu, Bolei Zhou, Yuning Jiang, and Jian Sun. Unified perceptual parsing for scene understanding. In *Proceedings of the European conference on computer vision (ECCV)*, pages 418–434, 2018.
- [44] Rui Xu, Shu Yang, Yihui Wang, Bo Du, and Hao Chen. A survey on vision mamba: Models, applications and challenges. *arXiv preprint arXiv:2404.18861*, 2024.
- [45] Chenyu Yi, Siyuan Yang, Haoliang Li, Yap-peng Tan, and Alex Kot. Benchmarking the robustness of spatial-temporal models against corruptions. *arXiv preprint arXiv:2110.06513*, 2021.
- [46] Yubiao Yue and Zhenzhang Li. Medmamba: Vision mamba for medical image classification. *arXiv preprint arXiv:2403.03849*, 2024.
- [47] Hongyang Zhang, Yaodong Yu, Jiantao Jiao, Eric Xing, Laurent El Ghaoui, and Michael Jordan. Theoretically principled trade-off between robustness and accuracy. In *International conference on machine learning*, pages 7472–7482. PMLR, 2019.

- [48] Bolei Zhou, Hang Zhao, Xavier Puig, Sanja Fidler, Adela Barriuso, and Antonio Torralba. Scene parsing through ade20k dataset. In *Proceedings of the IEEE conference on computer vision and pattern recognition*, pages 633–641, 2017.
- [49] Daquan Zhou, Zhiding Yu, Enze Xie, Chaowei Xiao, Animashree Anandkumar, Jiashi Feng, and Jose M Alvarez. Understanding the robustness in vision transformers. In *International Conference on Machine Learning*, pages 27378–27394. PMLR, 2022.
- [50] Lianghui Zhu, Bencheng Liao, Qian Zhang, Xinlong Wang, Wenyu Liu, and Xinggang Wang. Vision mamba: Efficient visual representation learning with bidirectional state space model. *arXiv preprint arXiv:2401.09417*, 2024.

Appendix

We offer further insights into our study through various sections in the appendix, incorporating both versions of the VSSM models[28], v2 (reported in the main paper) and v0. Firstly, we expand our analysis on adversarial attacks across recent CNN and Transformer models in Section A, presenting results for white-box and transfer-based black-box attacks. In Section B, we provide detailed results on non-adversarial corruptions. Section B.1 explores information drop along the scanning direction. Sections B.2 and B.4 offer additional detailed results on Salient and Non-Salient Patch Drop and Random Patch Drop, respectively. Section B.3 presents further results on patch shuffling. Additionally, Section B.5 provides results on ImageNet-E, ImageNet-B, ImageNet-V2, ImageNet-A, ImageNet-R, and ImageNet-S. In Section B.6, we report results for each common corruption method across different models.

A Adversarial Transferability

In this section, we expand our analysis on adversarial attacks and their transferability across different models. We include more model families, such as DeiT, DenseNet, and VGG. Figures 6, 7, and 8 present the robust accuracy of various models under both white-box and black-box settings for FGSM, PGD, and MIFGSM attacks, respectively. All adversarial examples are crafted with a perturbation budget of $\epsilon = \frac{8}{255}$. For PGD and MIFGSM attacks, we use 20 iterations to craft the adversarial examples.

Transferability Results for FGSM at Epsilon 8/255

| | VSSM-T_v2 | VSSM-S_v2 | VSSM-B_v2 | VSSM-T_v0 | VSSM-S_v0 | VSSM-B_v0 | ResNet-18 | ResNet-50 | VGG-16 | VGG-19 | DenseNet-121 | DenseNet-161 | ConvNext-T | ConvNext-S | ConvNext-B | ViT-T | ViT-S | ViT-B | DeiT-T | DeiT-S | DeiT-B | Swin-T | Swin-S | Swin-B |
|--------------|-----------|-----------|-----------|-----------|-----------|-----------|-----------|-----------|--------|--------|--------------|--------------|------------|------------|------------|-------|-------|-------|--------|--------|--------|--------|--------|--------|
| VSSM-T_v2 | 42.90 | 66.34 | 65.10 | 72.12 | 75.24 | 74.42 | 69.66 | 80.20 | 67.74 | 69.24 | 76.30 | 72.66 | 73.80 | 72.84 | 79.46 | 83.64 | 86.94 | 75.76 | 82.00 | 82.32 | 72.22 | 76.38 | 74.60 | |
| VSSM-S_v2 | 62.24 | 48.42 | 63.00 | 69.40 | 71.34 | 70.78 | 68.66 | 79.70 | 66.28 | 67.44 | 75.26 | 75.14 | 71.40 | 71.04 | 70.18 | 78.42 | 81.56 | 84.58 | 75.96 | 80.30 | 80.22 | 70.96 | 72.92 | 71.14 |
| VSSM-B_v2 | 65.52 | 66.96 | 51.24 | 72.50 | 74.38 | 72.94 | 70.04 | 81.22 | 68.62 | 69.56 | 77.34 | 76.84 | 73.54 | 73.20 | 72.32 | 79.12 | 83.62 | 86.24 | 76.20 | 81.58 | 81.82 | 73.24 | 76.30 | 73.88 |
| VSSM-T_v0 | 77.74 | 78.94 | 79.34 | 55.68 | 73.88 | 73.30 | 73.60 | 84.70 | 74.40 | 75.12 | 79.64 | 80.78 | 78.04 | 78.78 | 78.74 | 80.62 | 85.28 | 88.08 | 78.22 | 83.60 | 84.26 | 75.08 | 77.28 | 77.24 |
| VSSM-S_v0 | 76.50 | 77.10 | 77.20 | 70.82 | 58.28 | 71.52 | 72.22 | 83.54 | 72.68 | 73.04 | 78.42 | 79.06 | 76.34 | 76.12 | 76.00 | 79.72 | 82.92 | 85.62 | 76.88 | 81.78 | 82.68 | 74.22 | 75.82 | 74.84 |
| VSSM-B_v0 | 76.66 | 76.96 | 76.46 | 71.48 | 72.56 | 59.18 | 72.42 | 83.84 | 72.90 | 73.96 | 79.90 | 79.90 | 77.04 | 77.14 | 76.30 | 80.32 | 84.74 | 86.38 | 78.48 | 82.88 | 82.68 | 74.52 | 76.34 | 75.30 |
| ResNet-18 | 85.48 | 88.34 | 89.24 | 84.48 | 88.74 | 89.40 | 1.50 | 71.46 | 51.34 | 51.98 | 57.74 | 63.34 | 84.84 | 87.06 | 88.66 | 74.12 | 85.98 | 91.00 | 70.20 | 85.42 | 89.36 | 82.94 | 88.14 | 88.16 |
| ResNet-50 | 81.36 | 83.24 | 83.84 | 80.56 | 85.22 | 85.36 | 55.88 | 30.46 | 60.84 | 61.44 | 61.22 | 66.36 | 80.30 | 82.20 | 83.38 | 75.94 | 84.74 | 89.12 | 72.18 | 84.12 | 87.54 | 80.64 | 85.00 | 85.42 |
| VGG-16 | 83.80 | 86.80 | 87.42 | 85.72 | 89.74 | 89.82 | 58.10 | 80.84 | 2.92 | 37.80 | 73.40 | 74.42 | 83.82 | 86.24 | 87.34 | 80.42 | 89.42 | 92.98 | 76.10 | 89.16 | 91.92 | 83.52 | 88.78 | 88.48 |
| VGG-19 | 83.92 | 86.80 | 87.14 | 85.68 | 89.44 | 89.30 | 57.50 | 79.24 | 36.16 | 4.54 | 71.66 | 72.30 | 83.70 | 85.66 | 86.86 | 79.60 | 88.86 | 92.24 | 75.80 | 88.36 | 91.70 | 83.70 | 88.64 | 88.46 |
| DenseNet-121 | 85.42 | 87.82 | 88.80 | 84.68 | 88.10 | 88.84 | 54.10 | 71.70 | 62.36 | 63.40 | 15.36 | 64.58 | 84.06 | 86.14 | 88.00 | 76.38 | 85.96 | 90.72 | 72.52 | 86.28 | 89.74 | 83.34 | 88.32 | 88.72 |
| DenseNet-161 | 79.60 | 82.02 | 82.94 | 79.22 | 83.30 | 83.44 | 52.12 | 68.46 | 55.24 | 57.54 | 55.58 | 8.74 | 78.46 | 80.04 | 81.42 | 72.88 | 82.78 | 88.22 | 71.48 | 82.86 | 86.18 | 78.24 | 83.68 | 84.04 |
| ConvNext-T | 69.00 | 71.46 | 71.18 | 68.56 | 71.82 | 70.64 | 67.60 | 77.96 | 65.22 | 65.54 | 72.54 | 72.56 | 36.36 | 61.96 | 63.76 | 76.92 | 82.74 | 85.58 | 74.10 | 79.88 | 80.78 | 67.06 | 71.88 | 70.78 |
| ConvNext-S | 69.54 | 70.62 | 70.48 | 69.90 | 71.66 | 70.74 | 70.70 | 79.48 | 68.44 | 69.78 | 74.68 | 74.16 | 63.48 | 49.10 | 63.62 | 78.48 | 82.94 | 85.02 | 75.70 | 80.36 | 81.16 | 69.24 | 71.54 | 69.74 |
| ConvNext-B | 70.54 | 71.78 | 69.78 | 71.46 | 73.32 | 71.44 | 71.42 | 81.72 | 69.84 | 71.28 | 77.20 | 76.72 | 67.34 | 66.24 | 51.32 | 80.26 | 83.98 | 86.22 | 77.50 | 82.64 | 81.36 | 69.86 | 73.44 | 70.84 |
| ViT-T | 85.92 | 88.30 | 88.88 | 81.76 | 84.92 | 85.86 | 64.86 | 82.68 | 68.24 | 70.78 | 74.24 | 76.88 | 85.08 | 86.56 | 88.06 | 2.28 | 50.04 | 69.90 | 39.14 | 52.44 | 66.72 | 75.66 | 79.72 | 82.32 |
| ViT-S | 81.74 | 83.76 | 84.46 | 77.56 | 80.64 | 80.92 | 66.62 | 81.70 | 68.32 | 70.58 | 73.70 | 76.28 | 82.34 | 82.78 | 84.38 | 45.40 | 11.02 | 54.82 | 51.84 | 55.50 | 60.90 | 72.50 | 75.98 | 77.88 |
| ViT-B | 82.46 | 84.02 | 84.48 | 79.30 | 81.40 | 80.80 | 69.00 | 81.90 | 69.34 | 71.82 | 75.10 | 76.44 | 82.04 | 82.24 | 83.62 | 58.50 | 53.84 | 24.24 | 62.14 | 64.80 | 65.64 | 75.82 | 77.62 | 78.54 |
| DeiT-T | 83.34 | 86.40 | 87.74 | 77.82 | 82.88 | 83.74 | 61.36 | 80.06 | 64.82 | 67.28 | 69.86 | 75.44 | 82.06 | 84.40 | 86.68 | 38.14 | 58.42 | 73.58 | 10.96 | 42.92 | 59.50 | 70.86 | 77.84 | 80.68 |
| DeiT-S | 80.68 | 82.72 | 82.22 | 75.96 | 78.62 | 79.28 | 68.68 | 81.28 | 70.58 | 71.98 | 74.94 | 77.34 | 80.18 | 80.78 | 82.46 | 55.94 | 61.74 | 71.36 | 51.70 | 31.60 | 58.74 | 71.56 | 74.16 | 76.02 |
| DeiT-B | 81.74 | 83.42 | 83.28 | 79.56 | 81.86 | 80.90 | 70.62 | 83.50 | 71.34 | 74.14 | 77.46 | 79.28 | 81.92 | 83.00 | 83.42 | 65.16 | 70.62 | 75.38 | 61.40 | 64.84 | 42.16 | 76.52 | 78.42 | 78.84 |
| Swin-T | 72.40 | 76.06 | 75.58 | 67.86 | 72.58 | 71.80 | 70.32 | 82.82 | 70.50 | 71.82 | 76.88 | 78.08 | 71.46 | 72.12 | 71.96 | 76.48 | 80.66 | 85.46 | 72.52 | 78.12 | 80.16 | 68.86 | 56.22 | 55.12 |
| Swin-S | 78.24 | 79.10 | 79.30 | 73.96 | 76.84 | 75.86 | 74.24 | 85.46 | 75.34 | 76.30 | 81.46 | 82.32 | 77.96 | 77.10 | 77.02 | 79.38 | 83.04 | 86.58 | 77.40 | 81.64 | 61.94 | 68.94 | 63.90 | 63.90 |
| Swin-B | 78.88 | 79.40 | 79.04 | 76.08 | 77.68 | 77.24 | 74.58 | 86.60 | 75.38 | 77.26 | 82.18 | 81.96 | 78.16 | 78.46 | 77.32 | 81.48 | 84.74 | 87.64 | 79.18 | 83.56 | 82.86 | 66.82 | 68.28 | 54.76 |

Figure 6: Robust accuracy of various architectures under white-box and black-box settings for FGSM attack. Adversarial examples are crafted at a perturbation budget $\epsilon = \frac{8}{255}$.

B Non Adversarial Analysis

B.1 Drop Along Scanning Direction

We investigate the models' behavior when information is dropped along the scanning directions. We consider three settings: (1) linearly increasing the amount of information dropped in each patch along the scanning direction, with the most information dropped in patches that are traversed last by the scanning operation, (2) dropping most of the information in the center of the scanning directions while preserving most of the information in patches that are traversed at the beginning and the end, and (3) sequentially dropping patches along the scanning directions. In Figure 9 we show qualitative samples for showing information drop along scanning directions. Figure 10 we report results across the first experiment setting across all the scanning directions. In Figure 11 we report results for the second experiment setting. Furthermore, in Figure 12 we report results across the third experiment setting across all the scanning directions.

B.2 DINO Drop

In Figure 13 and 14, we report results on salient and non-salient patch drop of information.

Transferability Results for PGD at Epsilon 8/255

| | VSSM-T_v2 | VSSM-S_v2 | VSSM-B_v2 | VSSM-T_v0 | VSSM-S_v0 | VSSM-B_v0 | ResNet-18 | ResNet-50 | VGG-16 | VGG-19 | DenseNet-121 | DenseNet-161 | ConvNext-T | ConvNext-S | ConvNext-B | ViT-T | ViT-S | ViT-B | DeiT-T | DeiT-S | DeiT-B | Swin-T | Swin-S | Swin-B |
|--------------|-----------|-----------|-----------|-----------|-----------|-----------|-----------|-----------|--------|--------|--------------|--------------|------------|------------|------------|-------|-------|-------|--------|--------|--------|--------|--------|--------|
| VSSM-T_v2 | 0.00 | 37.26 | 35.56 | 64.48 | 73.60 | 70.60 | 69.58 | 81.44 | 54.40 | 57.86 | 75.30 | 77.72 | 63.54 | 67.18 | 65.88 | 82.58 | 89.16 | 91.80 | 78.82 | 87.98 | 89.02 | 65.76 | 74.72 | 71.50 |
| VSSM-S_v2 | 16.88 | 0.02 | 23.94 | 53.54 | 60.70 | 58.56 | 65.14 | 77.54 | 45.10 | 48.76 | 70.98 | 72.44 | 56.24 | 57.72 | 56.16 | 79.26 | 86.08 | 89.42 | 76.46 | 85.26 | 86.02 | 58.92 | 65.92 | 61.46 |
| VSSM-B_v2 | 15.98 | 25.26 | 0.00 | 54.46 | 63.08 | 58.60 | 65.72 | 77.38 | 44.18 | 48.36 | 70.88 | 72.30 | 56.30 | 57.94 | 53.42 | 79.76 | 86.24 | 89.94 | 75.68 | 85.08 | 85.96 | 57.40 | 66.52 | 61.74 |
| VSSM-T_v0 | 71.14 | 75.74 | 75.30 | 0.72 | 53.94 | 51.38 | 71.56 | 83.84 | 65.42 | 67.22 | 76.94 | 80.16 | 69.12 | 71.16 | 72.26 | 81.16 | 87.74 | 91.34 | 77.44 | 87.12 | 88.90 | 58.96 | 67.66 | 67.34 |
| VSSM-S_v0 | 63.50 | 66.08 | 66.50 | 27.90 | 0.32 | 35.78 | 68.84 | 79.44 | 58.16 | 60.44 | 72.32 | 75.74 | 59.74 | 58.68 | 60.84 | 78.30 | 84.62 | 89.16 | 74.66 | 84.10 | 86.04 | 49.70 | 56.82 | 55.90 |
| VSSM-B_v0 | 61.42 | 65.24 | 63.00 | 25.50 | 37.36 | 0.40 | 68.64 | 80.96 | 58.46 | 61.06 | 73.90 | 76.92 | 59.60 | 61.08 | 59.96 | 79.16 | 85.18 | 89.48 | 74.82 | 84.36 | 85.52 | 46.96 | 55.02 | 53.64 |
| ResNet-18 | 87.54 | 91.08 | 91.44 | 87.32 | 91.64 | 91.62 | 0.00 | 68.62 | 44.76 | 46.56 | 49.88 | 59.30 | 86.20 | 89.28 | 91.30 | 79.84 | 89.76 | 93.88 | 76.02 | 90.10 | 92.80 | 85.40 | 91.04 | 91.36 |
| ResNet-50 | 83.34 | 86.98 | 87.04 | 85.02 | 88.28 | 89.02 | 56.82 | 0.00 | 58.12 | 59.18 | 52.36 | 63.78 | 81.00 | 84.92 | 86.30 | 82.48 | 89.96 | 93.18 | 78.36 | 89.64 | 92.10 | 84.18 | 89.24 | 89.12 |
| VGG-16 | 86.12 | 89.18 | 88.64 | 88.56 | 92.34 | 92.42 | 65.82 | 85.62 | 0.06 | 13.12 | 79.36 | 80.14 | 85.50 | 87.94 | 88.54 | 85.44 | 92.56 | 95.02 | 81.36 | 93.16 | 94.36 | 86.72 | 92.14 | 91.18 |
| VGG-19 | 86.24 | 88.86 | 89.30 | 88.30 | 92.04 | 92.28 | 63.98 | 82.94 | 10.32 | 0.08 | 76.64 | 77.64 | 84.22 | 87.28 | 88.54 | 85.20 | 92.62 | 94.94 | 80.92 | 92.66 | 94.38 | 87.24 | 91.06 | 91.08 |
| DenseNet-121 | 87.28 | 89.86 | 90.12 | 86.32 | 89.76 | 90.72 | 51.48 | 68.44 | 61.58 | 61.86 | 0.00 | 57.60 | 84.38 | 87.48 | 89.94 | 81.10 | 89.42 | 93.12 | 76.94 | 89.96 | 92.32 | 85.56 | 89.84 | 90.56 |
| DenseNet-161 | 74.68 | 78.60 | 79.46 | 76.30 | 81.34 | 81.78 | 45.12 | 57.88 | 45.18 | 45.86 | 34.72 | 0.20 | 70.72 | 74.80 | 77.26 | 77.10 | 85.90 | 89.74 | 73.86 | 85.86 | 88.14 | 75.72 | 82.64 | 82.12 |
| ConvNext-T | 60.58 | 67.06 | 66.48 | 58.20 | 67.44 | 64.30 | 68.08 | 79.76 | 53.76 | 55.30 | 71.80 | 73.14 | 0.00 | 31.32 | 39.70 | 80.44 | 87.28 | 90.46 | 77.54 | 86.30 | 87.76 | 66.62 | 66.62 | 64.40 |
| ConvNext-S | 58.04 | 63.20 | 62.96 | 54.98 | 60.98 | 60.10 | 66.38 | 78.22 | 51.06 | 53.68 | 70.30 | 71.26 | 24.96 | 0.00 | 33.96 | 80.02 | 86.20 | 89.86 | 76.24 | 85.52 | 86.24 | 52.70 | 62.58 | 60.54 |
| ConvNext-B | 58.24 | 64.04 | 60.40 | 57.52 | 63.96 | 61.60 | 69.66 | 80.80 | 54.66 | 57.78 | 75.02 | 74.84 | 35.84 | 36.60 | 0.00 | 91.48 | 87.22 | 90.36 | 78.42 | 87.08 | 87.42 | 51.80 | 61.16 | 58.62 |
| ViT-T | 92.10 | 93.82 | 94.26 | 88.98 | 91.46 | 92.08 | 71.20 | 88.14 | 75.06 | 76.38 | 80.42 | 83.96 | 90.44 | 92.16 | 93.28 | 0.00 | 55.58 | 77.34 | 40.00 | 60.24 | 76.88 | 84.52 | 88.16 | 89.24 |
| ViT-S | 87.28 | 89.34 | 89.70 | 82.82 | 85.64 | 86.44 | 70.82 | 85.96 | 73.26 | 74.66 | 77.96 | 81.76 | 86.34 | 87.90 | 89.26 | 38.16 | 0.00 | 48.68 | 49.94 | 54.22 | 64.28 | 76.98 | 80.34 | 82.48 |
| ViT-B | 86.18 | 87.74 | 87.72 | 81.58 | 84.06 | 84.56 | 71.28 | 85.04 | 73.58 | 74.40 | 77.90 | 80.46 | 85.56 | 86.10 | 87.62 | 53.50 | 37.48 | 0.00 | 60.42 | 63.04 | 62.64 | 77.02 | 79.56 | 80.86 |
| DeiT-T | 91.32 | 93.16 | 93.74 | 88.26 | 90.92 | 92.02 | 68.38 | 86.62 | 72.16 | 73.28 | 77.58 | 83.42 | 90.20 | 91.90 | 93.44 | 37.02 | 65.62 | 81.82 | 0.00 | 43.00 | 68.42 | 82.34 | 87.90 | 89.38 |
| DeiT-S | 86.30 | 88.90 | 89.68 | 81.02 | 84.82 | 85.38 | 69.20 | 85.36 | 72.46 | 73.44 | 76.80 | 81.28 | 85.24 | 87.68 | 89.24 | 41.74 | 54.94 | 73.10 | 28.18 | 0.00 | 44.44 | 74.74 | 82.58 | 81.74 |
| DeiT-B | 84.70 | 87.28 | 87.86 | 79.92 | 82.82 | 83.48 | 69.98 | 85.40 | 72.24 | 73.68 | 76.96 | 81.22 | 84.00 | 85.56 | 87.14 | 57.84 | 64.08 | 71.70 | 48.68 | 44.12 | 0.00 | 74.50 | 78.28 | 79.34 |
| Swin-T | 83.10 | 87.58 | 87.02 | 74.72 | 82.30 | 80.16 | 76.00 | 89.58 | 74.12 | 76.22 | 84.08 | 86.00 | 79.30 | 81.52 | 80.28 | 83.32 | 89.82 | 92.80 | 79.58 | 88.62 | 90.56 | 0.00 | 39.00 | 37.88 |
| Swin-S | 83.08 | 86.28 | 86.26 | 72.52 | 80.18 | 78.80 | 76.58 | 89.76 | 74.90 | 76.20 | 84.34 | 86.44 | 79.60 | 80.68 | 79.84 | 82.96 | 88.80 | 92.38 | 79.80 | 88.34 | 89.84 | 25.40 | 0.00 | 31.44 |
| Swin-B | 82.52 | 85.12 | 84.78 | 74.02 | 81.04 | 78.68 | 76.44 | 89.88 | 73.28 | 75.36 | 85.24 | 86.80 | 79.18 | 80.08 | 78.92 | 84.24 | 89.74 | 92.86 | 81.30 | 89.26 | 90.12 | 27.30 | 34.36 | 0.02 |

Figure 7: Robust accuracy of various architectures under white-box and black-box settings for PGD attack. Adversarial examples are crafted at a perturbation budget $\epsilon = \frac{8}{255}$.

Transferability Results for MIFGSM at Epsilon 8/255

| | VSSM-T_v2 | VSSM-S_v2 | VSSM-B_v2 | VSSM-T_v0 | VSSM-S_v0 | VSSM-B_v0 | ResNet-18 | ResNet-50 | VGG-16 | VGG-19 | DenseNet-121 | DenseNet-161 | ConvNext-T | ConvNext-S | ConvNext-B | ViT-T | ViT-S | ViT-B | DeiT-T | DeiT-S | DeiT-B | Swin-T | Swin-S | Swin-B |
|--------------|-----------|-----------|-----------|-----------|-----------|-----------|-----------|-----------|--------|--------|--------------|--------------|------------|------------|------------|-------|-------|-------|--------|--------|--------|--------|--------|--------|
| VSSM-T_v2 | 0.00 | 25.98 | 24.92 | 52.08 | 60.62 | 58.12 | 61.40 | 71.54 | 46.10 | 49.04 | 67.08 | 67.76 | 50.82 | 53.96 | 51.98 | 76.42 | 81.64 | 86.56 | 71.92 | 80.82 | 81.12 | 53.78 | 64.04 | 60.42 |
| VSSM-S_v2 | 12.46 | 0.00 | 16.98 | 40.32 | 46.72 | 44.42 | 55.16 | 65.62 | 36.18 | 40.58 | 60.34 | 58.90 | 42.32 | 43.14 | 42.28 | 71.84 | 76.92 | 82.58 | 67.78 | 75.24 | 76.08 | 46.86 | 53.04 | 49.54 |
| VSSM-B_v2 | 12.90 | 18.50 | 0.00 | 42.72 | 50.88 | 46.12 | 56.54 | 67.94 | 36.50 | 41.04 | 62.00 | 61.26 | 43.82 | 45.70 | 41.18 | 72.82 | 78.54 | 83.54 | 68.50 | 77.04 | 77.28 | 47.12 | 55.76 | 50.32 |
| VSSM-T_v0 | 59.86 | 63.26 | 63.04 | 0.00 | 44.14 | 42.98 | 64.84 | 76.82 | 60.32 | 62.28 | 69.80 | 72.48 | 57.82 | 58.60 | 60.20 | 74.98 | 81.18 | 85.80 | 71.04 | 78.46 | 80.74 | 50.80 | 57.62 | 56.68 |
| VSSM-S_v0 | 50.74 | 52.68 | 53.06 | 22.84 | 0.04 | 26.14 | 60.38 | 71.66 | 52.62 | 53.94 | 63.54 | 65.84 | 48.94 | 45.14 | 47.14 | 70.62 | 75.90 | 82.38 | 66.60 | 73.42 | 75.66 | 39.82 | 46.14 | 44.72 |
| VSSM-B_v0 | 48.90 | 50.46 | 48.94 | 20.80 | 26.24 | 0.02 | 60.30 | 72.68 | 49.90 | 52.60 | 65.86 | 66.90 | 46.60 | 47.72 | 46.90 | 71.42 | 77.90 | 82.80 | 68.04 | 75.16 | 76.24 | 37.74 | 45.26 | 43.44 |
| ResNet-18 | 82.26 | 85.36 | 86.50 | 81.90 | 86.70 | 87.60 | 0.00 | 58.10 | 34.42 | 36.24 | 38.94 | 46.58 | 80.26 | 83.98 | 86.60 | 71.20 | 84.92 | 90.38 | 68.20 | 84.80 | 89.28 | 79.56 | 86.46 | 87.14 |
| ResNet-50 | 73.02 | 76.76 | 77.84 | 75.32 | 80.22 | 80.78 | 42.86 | 0.02 | 45.18 | 46.28 | 38.78 | 48.32 | 72.02 | 75.62 | 77.76 | 73.32 | 82.56 | 88.16 | 68.78 | 83.22 | 86.44 | 75.32 | 81.96 | 82.26 |
| VGG-16 | 78.94 | 83.72 | 83.52 | 83.52 | 88.52 | 88.38 | 55.24 | 77.46 | 0.10 | 8.74 | 71.58 | 70.18 | 78.68 | 82.04 | 83.12 | 80.52 | 89.44 | 93.04 | 75.90 | 89.58 | 92.78 | 80.84 | 87.66 | 87.48 |
| VGG-19 | 78.28 | 82.64 | 82.98 | 82.16 | 87.26 | 87.30 | 51.86 | 74.32 | 6.10 | 0.08 | 67.12 | 66.78 | 77.54 | 81.24 | 82.52 | 79.88 | 89.10 | 92.48 | 74.70 | 89.02 | 91.44 | 80.30 | 87.10 | 87.28 |
| DenseNet-121 | 80.42 | 84.10 | 84.72 | 80.20 | 84.52 | 85.54 | 38.82 | 56.54 | 49.74 | 51.16 | 0.00 | 44.26 | 78.58 | 81.78 | 84.36 | 73.24 | 83.98 | 89.80 | 69.74 | 84.50 | 87.92 | 78.42 | 85.90 | 85.66 |
| DenseNet-161 | 65.66 | 70.14 | 71.66 | 67.02 | 73.34 | 75.16 | 35.96 | 46.92 | 35.74 | 37.70 | 27.28 | 0.20 | 63.50 | 66.68 | 68.54 | 67.84 | 78.42 | 84.62 | 65.86 | 78.14 | 82.22 | 68.06 | 75.68 | 76.02 |
| ConvNext-T | 47.00 | 52.92 | 52.02 | 45.18 | 53.72 | 51.30 | 58.44 | 69.50 | 45.16 | 47.28 | 61.18 | 61.00 | 0.00 | 22.54 | 29.56 | 72.84 | 79.22 | 84.36 | 68.52 | 76.80 | 78.06 | 44.20 | 55.56 | 53.36 |
| ConvNext-S | 43.58 | 47.44 | 46.90 | 40.28 | 45.20 | 44.92 | 56.94 | 66.66 | 43.48 | 46.30 | 57.70 | 58.82 | 17.96 | 0.00 | 21.86 | 70.16 | 76.50 | 81.10 | 67.06 | 74.86 | 75.44 | 39.50 | 48.78 | 45.42 |
| ConvNext-B | 46.04 | 50.72 | 47.28 | 45.90 | 52.08 | 48.42 | 62.32 | 70.76 | 47.62 | 51.42 | 65.76 | 64.62 | 26.30 | 25.46 | 0.00 | 74.56 | 79.92 | 84.26 | 71.48 | 78.76 | 78.28 | 42.04 | 52.54 | 47.72 |
| ViT-T | 88.00 | 90.46 | 91.30 | 83.88 | 87.18 | 88.38 | 63.22 | 82.38 | 65.34 | 67.30 | 73.98 | 77.58 | 87.32 | 88.62 | 90.92 | 0.00 | 44.78 | 68.80 | 31.50 | 48.70 | 67.86 | 78.08 | 82.98 | 85.36 |
| ViT-S | 83.24 | 84.96 | 86.16 | 77.26 | 81.40 | 81.92 | 63.94 | 79.90 | 65.38 | 67.26 | 72.66 | 74.94 | 82.24 | 83.62 | 85.40 | 31.34 | 0.00 | 39.28 | 43.48 | 44.60 | 54.76 | 70.90 | 74.54 | 77.28 |
| ViT-B | 81.56 | 83.40 | 84.32 | 75.80 | 78.74 | 79.74 | 64.66 | 79.78 | 64.98 | 67.86 | 71.40 | 74.14 | 80.88 | 81.98 | | | | | | | | | | |

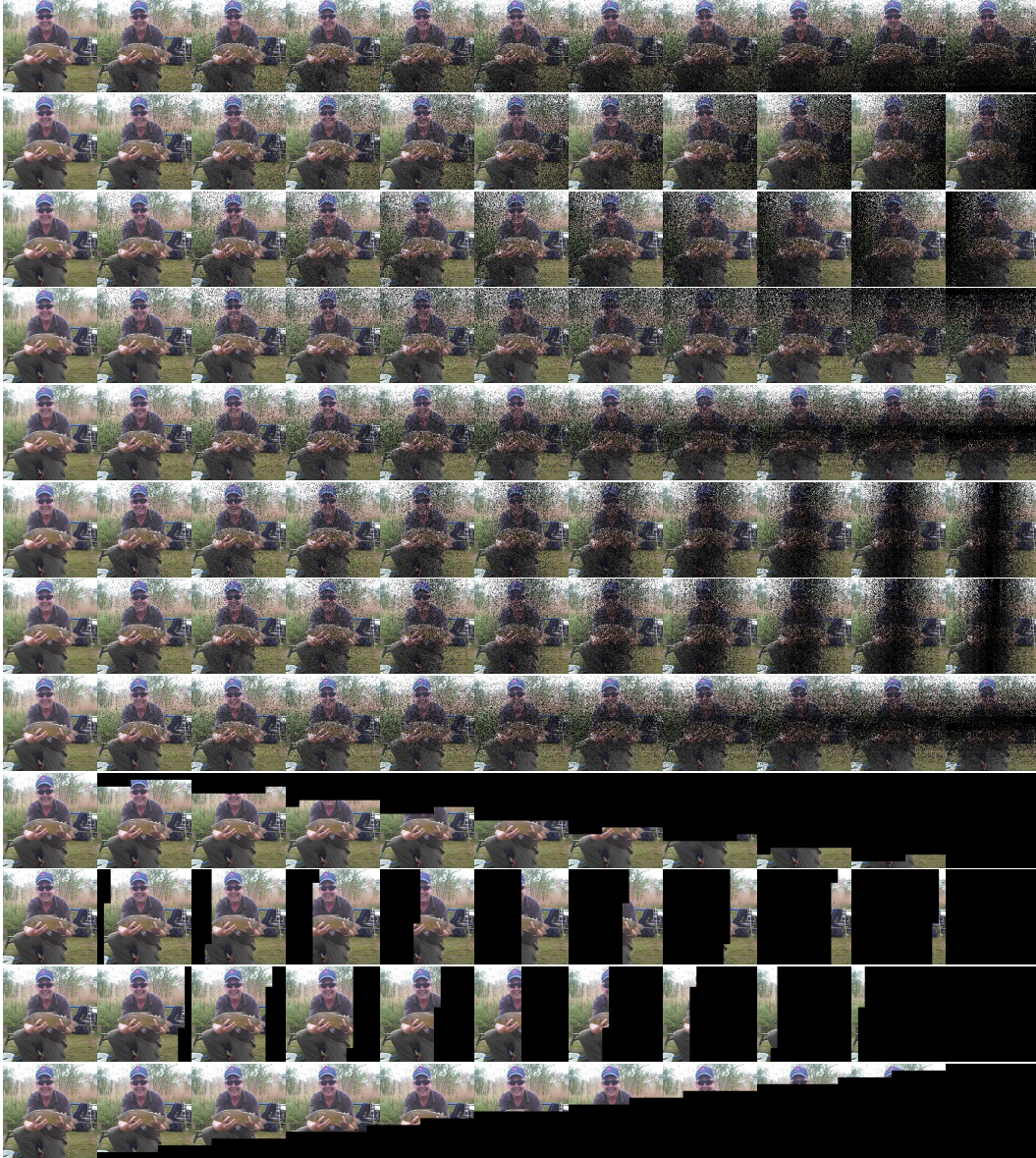


Figure 9: Information drop along scanning direction: The top four rows represent linearly increasing information drop along the four scanning directions at patch size 14×14 . The center four rows represent linearly increasing information drop till the center along the four scanning directions at patch size 14×14 . The bottom four rows represent sequentially dropping patches along the four scanning directions at patch size 14×14 .

to evaluate the robustness and generalization capabilities of models trained on the original ImageNet dataset. ImageNetV2 [41] tests the models’ performance on previously unseen images that follow the same distribution as the training data, while ImageNet-A [19] contains naturally occurring adversarial examples that are difficult for models to classify correctly. ImageNet-R [18] consists of images with different artistic renditions to test the models’ ability to generalize to different visual domains and styles, and ImageNet-S [11] introduces various types of synthetic corruptions to assess the models’ robustness against image distortions like noise, blur, and compression artifacts.

B.6 Common Corruptions

In Figure 22 and 23, we present the relative corruption error and mean corruption error (mCE) of various models subjected to all 19 corruption methods applied to the ImageNet dataset. Figure 24 shows the mIoU, mAcc, and aAcc scores on ADE-20K after applying common corruptions to the dataset. Similarly, Figure 25 displays the

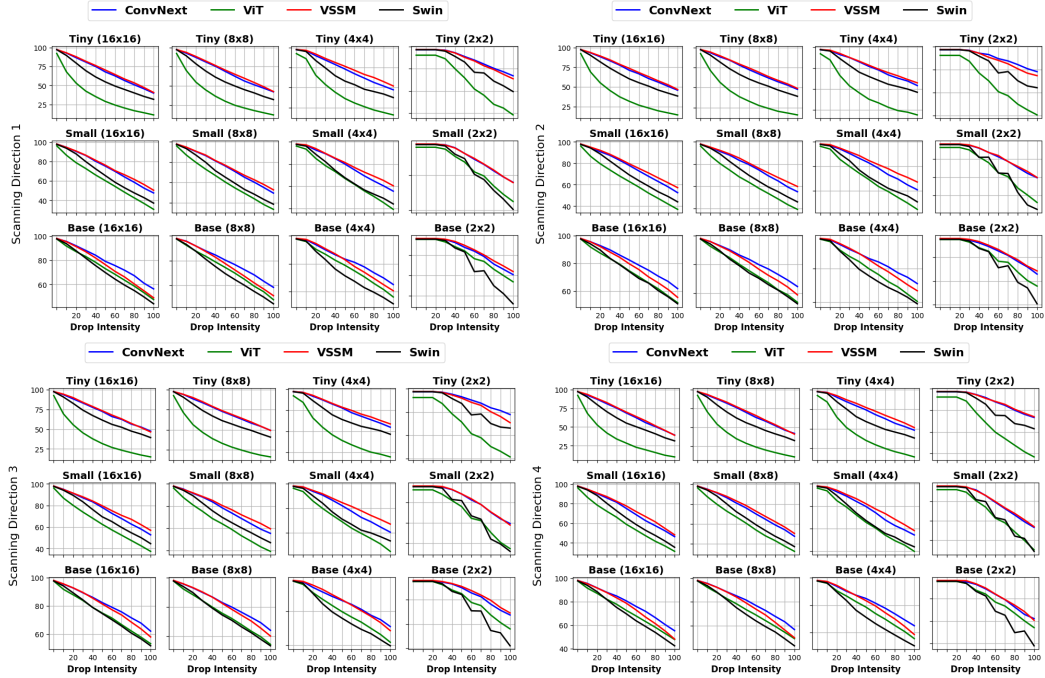


Figure 10: Information drop of Tiny and Small family of models along the scanning direction: the image is split into a sequence of fixed-size non-overlapping patches of size 16x16, 8x8, 4x4, and 2x2. We report results of linearly increasing the number of pixels dropped from each patch to the maximum threshold (*Drop Intensity*) along the scanning direction. The top row shows results for top-to-bottom (*Direction 1*) and left-to-right direction (*Direction 2*). The bottom row shows results for right-to-left (*Direction 3*) and bottom-to-top direction (*Direction 4*).

mAP, APs, APm, and API scores on the COCO-C dataset. All the scores are averaged across all severity levels of each corruption.

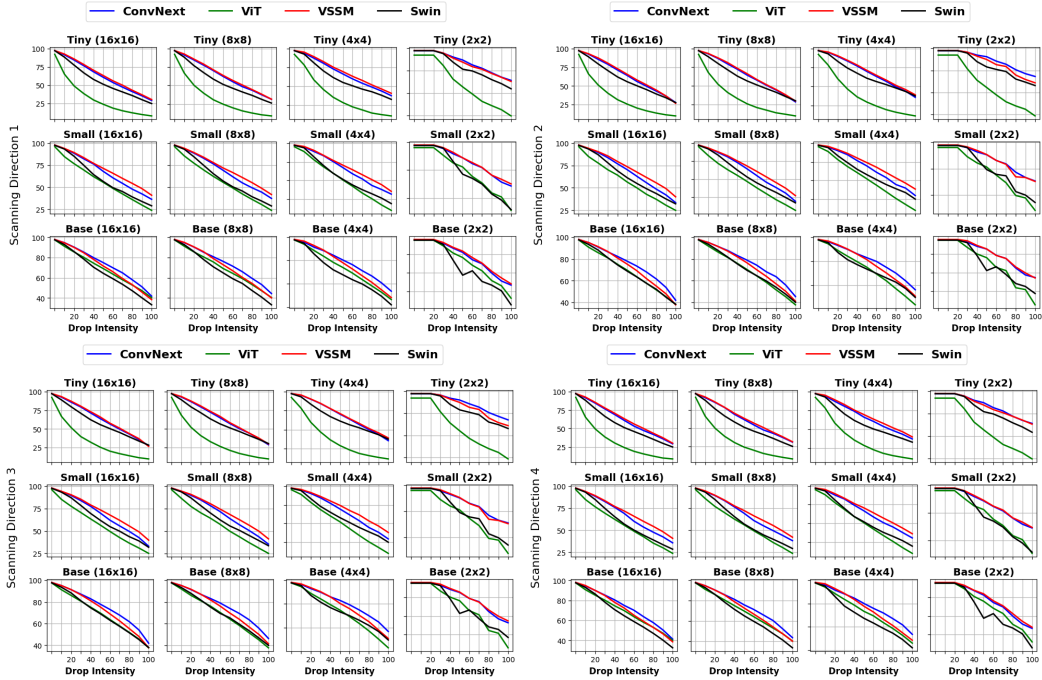


Figure 11: Information drop of Tiny and Small family of models along the scanning direction: the image is split into a sequence of fixed-size non-overlapping patches of size 16x16, 8x8, 4x4, and 2x2. We report results of linearly increasing the number of pixels dropped from each patch to the maximum threshold (*Drop Intensity*) at the center of the scanning direction and then again linearly decreased till the end. The top row shows results for top-to-bottom (*Direction 1*) and left-to-right direction (*Direction 2*). The bottom row shows results for right-to-left (*Direction 3*) and bottom-to-top direction (*Direction 4*).

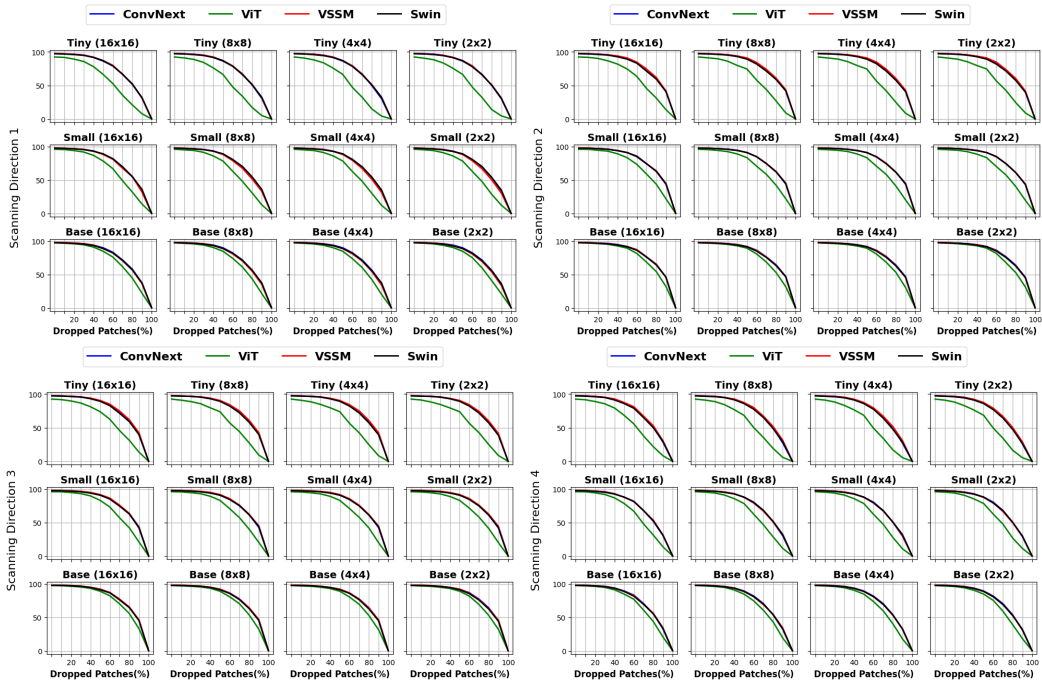


Figure 12: Information drop of Tiny and Small family of models along the scanning direction: the image is split into a sequence of fixed-size non-overlapping patches of size 16x16, 8x8, 4x4, and 2x2. We report results of sequentially dropping patches along the scanning direction. The top row shows results for top-to-bottom (*Direction 1*) and left-to-right direction (*Direction 2*). The bottom row shows results for right-to-left (*Direction 3*) and bottom-to-top direction (*Direction 4*).

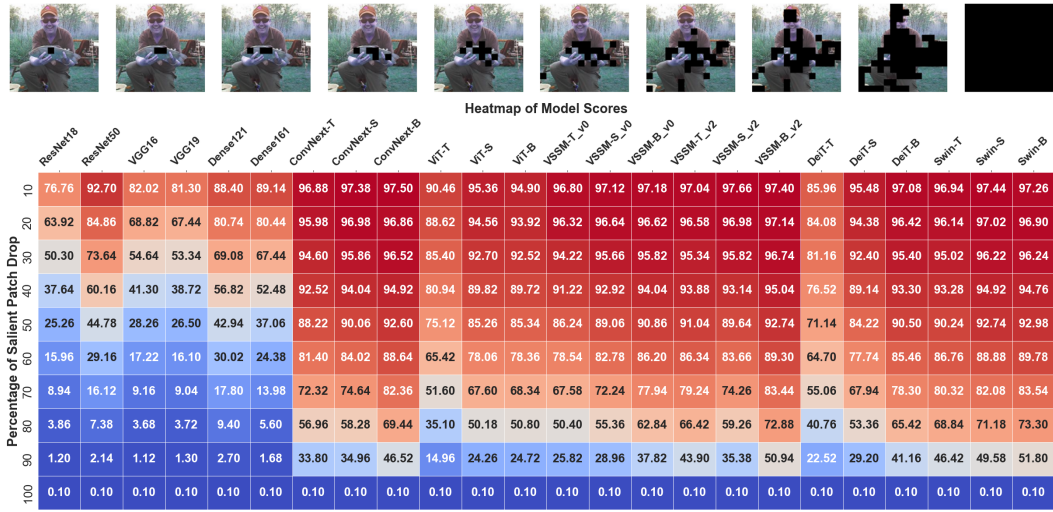


Figure 13: Top-1 classification accuracy reported under salient patch drop occlusion using 16×16 patch size.

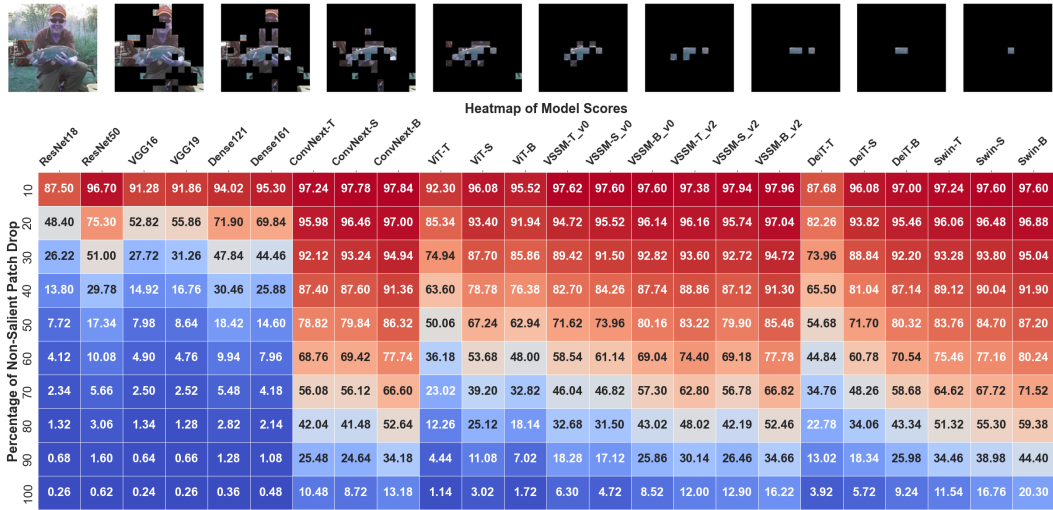


Figure 14: Top-1 classification accuracy reported under non-salient patch drop occlusion using 16×16 patch size.

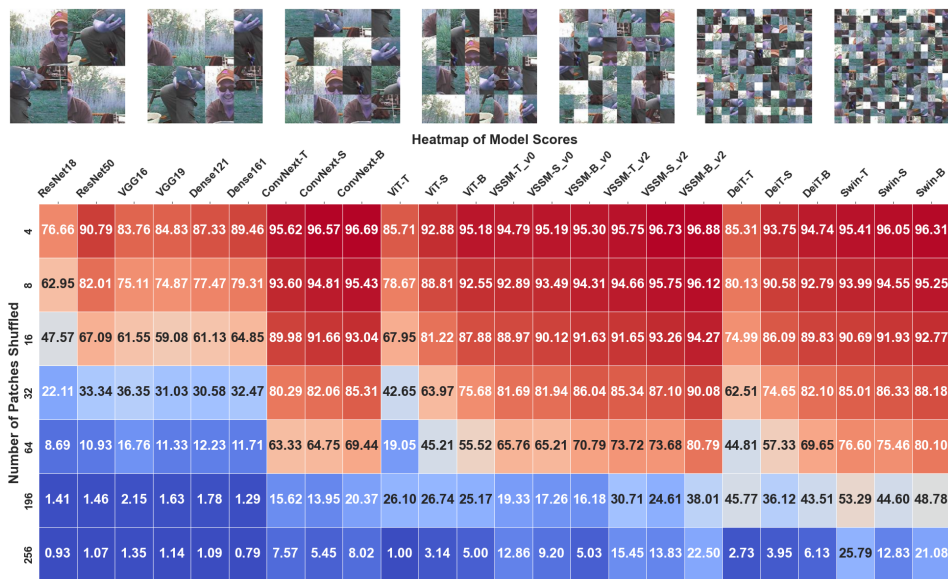


Figure 15: Top-1 classification accuracy among various architectures under increasing patch shuffling.

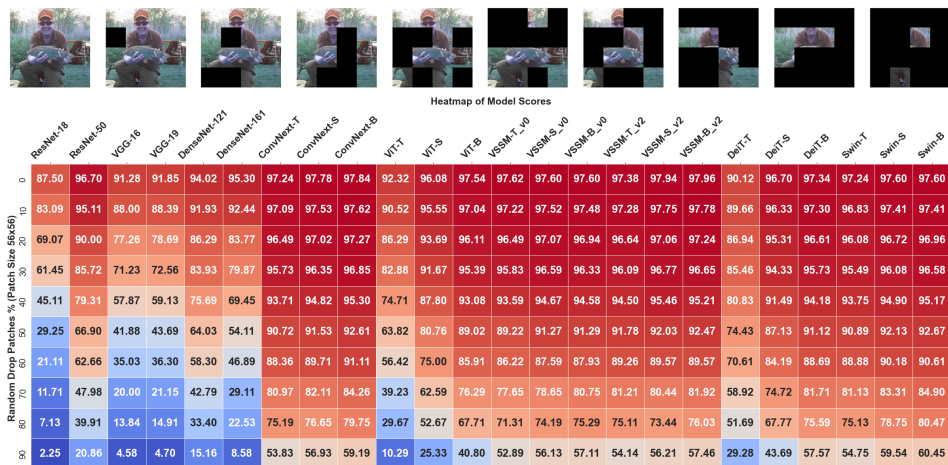


Figure 16: Top-1 classification accuracy of various architectures under random patch drop occlusions, using 56×56 patch size.

Table 9: Top-1 classification accuracy reported random patch drop occlusion using 16×16 , 8×8 , 4×4 and 1×1 patch sizes.

| ResNet-50 | ConvNext-T | ConvNext-S | ConvNext-B | ViT-T | ViT-S | ViT-B | VSSM-T | VSSM-S | VSSM-B | Swin-T | Swin-S | Swin-B |
|---|------------|------------|------------|-------|-------|-------|--------|--------|--------|--------|--------|--------|
| <i>Patch Size 16×16 (Percentage of patch drop increasing from top to bottom (10% to 90%))</i> | | | | | | | | | | | | |
| 96.70 | 97.24 | 97.78 | 97.84 | 92.30 | 96.08 | 97.54 | 97.38 | 97.94 | 97.96 | 97.24 | 97.60 | 97.60 |
| 75.27 | 96.49 | 97.19 | 97.37 | 90.83 | 95.39 | 96.85 | 96.49 | 96.61 | 97.25 | 96.76 | 97.38 | 97.32 |
| 39.93 | 94.63 | 95.27 | 96.48 | 88.09 | 94.29 | 96.27 | 95.16 | 92.97 | 96.25 | 96.11 | 96.84 | 96.79 |
| 17.91 | 89.99 | 91.12 | 95.29 | 85.26 | 92.35 | 95.08 | 93.45 | 89.74 | 95.21 | 94.88 | 95.88 | 96.17 |
| 6.73 | 81.43 | 84.63 | 93.03 | 80.08 | 90.15 | 92.78 | 90.52 | 84.82 | 93.46 | 93.38 | 94.35 | 95.03 |
| 2.43 | 70.07 | 74.44 | 88.76 | 72.49 | 85.10 | 89.21 | 86.52 | 78.41 | 90.89 | 91.05 | 92.21 | 93.25 |
| 1.05 | 57.59 | 60.15 | 82.35 | 61.34 | 76.56 | 82.08 | 80.52 | 68.40 | 87.03 | 87.96 | 87.84 | 90.43 |
| 0.56 | 44.67 | 44.71 | 71.25 | 45.63 | 62.63 | 70.25 | 70.39 | 52.72 | 79.96 | 80.65 | 79.71 | 84.70 |
| 0.45 | 31.29 | 28.82 | 57.71 | 25.86 | 41.73 | 50.08 | 56.23 | 34.51 | 67.56 | 70.37 | 66.60 | 74.38 |
| 0.43 | 16.73 | 14.98 | 33.67 | 7.85 | 15.86 | 19.68 | 34.83 | 16.82 | 41.55 | 47.16 | 47.85 | 53.54 |
| <i>Patch Size 8×8 (Percentage of patch drop increasing from top to bottom (10% to 90%))</i> | | | | | | | | | | | | |
| 96.70 | 97.24 | 97.78 | 97.84 | 92.32 | 96.08 | 97.54 | 97.38 | 97.94 | 97.96 | 97.24 | 97.60 | 97.60 |
| 44.91 | 86.69 | 91.39 | 95.63 | 70.18 | 88.90 | 94.23 | 87.86 | 85.93 | 90.20 | 96.44 | 96.77 | 96.76 |
| 12.44 | 68.38 | 81.13 | 90.83 | 42.19 | 79.72 | 88.37 | 79.91 | 78.23 | 84.43 | 95.04 | 94.87 | 95.84 |
| 3.79 | 55.12 | 68.35 | 84.08 | 16.91 | 65.39 | 76.63 | 70.40 | 70.95 | 78.47 | 92.87 | 92.08 | 94.49 |
| 1.35 | 39.05 | 54.58 | 73.51 | 4.59 | 46.17 | 60.12 | 57.34 | 59.09 | 70.04 | 90.13 | 88.21 | 92.40 |
| 0.56 | 23.89 | 37.94 | 58.05 | 1.25 | 25.91 | 39.97 | 43.09 | 44.08 | 58.29 | 85.40 | 81.87 | 88.36 |
| 0.33 | 13.33 | 21.97 | 40.37 | 0.45 | 11.03 | 21.56 | 28.25 | 27.85 | 43.00 | 78.76 | 71.63 | 81.85 |
| 0.21 | 5.95 | 9.85 | 21.51 | 0.21 | 3.78 | 8.85 | 14.69 | 12.45 | 25.75 | 68.40 | 53.81 | 70.03 |
| 0.24 | 2.08 | 2.31 | 7.85 | 0.14 | 1.02 | 2.49 | 5.11 | 2.45 | 10.07 | 52.41 | 29.58 | 49.35 |
| 0.25 | 0.46 | 0.56 | 1.33 | 0.16 | 0.39 | 0.59 | 0.75 | 0.43 | 1.65 | 28.46 | 8.32 | 23.67 |
| <i>Patch Size 4×4 (Percentage of patch drop increasing from top to bottom (10% to 90%))</i> | | | | | | | | | | | | |
| 96.70 | 97.24 | 97.78 | 97.84 | 92.30 | 96.08 | 97.54 | 97.38 | 97.94 | 97.96 | 97.24 | 97.60 | 97.60 |
| 30.11 | 84.75 | 88.74 | 90.51 | 29.62 | 82.23 | 90.04 | 86.34 | 87.17 | 90.48 | 92.51 | 92.97 | 94.68 |
| 12.02 | 64.23 | 77.49 | 81.82 | 9.25 | 65.28 | 77.00 | 72.09 | 75.43 | 77.77 | 84.20 | 86.17 | 90.71 |
| 6.49 | 33.19 | 47.91 | 70.73 | 3.63 | 43.92 | 56.17 | 51.01 | 55.23 | 53.83 | 72.07 | 77.69 | 85.35 |
| 2.91 | 13.34 | 19.71 | 54.95 | 1.58 | 21.73 | 32.19 | 27.17 | 33.21 | 29.41 | 57.71 | 65.13 | 78.48 |
| 1.46 | 5.17 | 6.67 | 34.97 | 0.70 | 8.96 | 15.24 | 10.51 | 15.82 | 11.57 | 41.57 | 47.95 | 69.11 |
| 0.75 | 2.07 | 2.23 | 17.37 | 0.41 | 3.69 | 6.01 | 3.07 | 5.41 | 3.40 | 26.49 | 29.31 | 54.59 |
| 0.40 | 0.85 | 0.90 | 6.21 | 0.24 | 1.45 | 1.91 | 0.83 | 1.28 | 0.63 | 12.17 | 12.45 | 35.95 |
| 0.21 | 0.33 | 0.44 | 1.70 | 0.17 | 0.55 | 0.71 | 0.23 | 0.30 | 0.24 | 3.48 | 2.47 | 14.47 |
| 0.13 | 0.20 | 0.25 | 0.40 | 0.19 | 0.24 | 0.25 | 0.19 | 0.21 | 0.22 | 0.64 | 0.41 | 1.55 |
| <i>Patch Size 1×1 (Percentage of patch drop increasing from top to bottom (10% to 90%))</i> | | | | | | | | | | | | |
| 96.70 | 97.24 | 97.78 | 97.84 | 92.32 | 96.08 | 97.54 | 97.38 | 97.94 | 97.96 | 97.24 | 97.60 | 97.60 |
| 54.40 | 83.43 | 87.12 | 89.68 | 47.56 | 76.30 | 85.64 | 85.87 | 89.55 | 89.73 | 74.40 | 85.10 | 85.14 |
| 37.39 | 69.17 | 76.25 | 79.47 | 27.12 | 61.71 | 75.93 | 71.95 | 77.99 | 79.11 | 48.34 | 63.30 | 62.51 |
| 26.21 | 53.81 | 62.42 | 68.38 | 15.67 | 47.69 | 65.85 | 56.63 | 64.54 | 66.81 | 33.44 | 45.94 | 49.32 |
| 17.80 | 38.14 | 45.85 | 58.50 | 9.02 | 34.97 | 55.16 | 43.11 | 52.29 | 54.38 | 25.06 | 32.73 | 39.90 |
| 11.85 | 26.13 | 31.79 | 47.28 | 5.11 | 23.24 | 43.27 | 32.61 | 41.20 | 42.08 | 18.84 | 23.16 | 31.09 |
| 7.19 | 17.81 | 21.99 | 35.81 | 2.78 | 14.30 | 31.58 | 23.08 | 30.97 | 29.57 | 12.75 | 15.41 | 22.05 |
| 3.94 | 11.18 | 15.01 | 21.95 | 1.39 | 7.82 | 19.59 | 13.39 | 21.11 | 17.70 | 6.69 | 9.58 | 11.99 |
| 1.79 | 4.47 | 8.49 | 9.15 | 0.61 | 3.51 | 10.46 | 4.65 | 9.64 | 6.79 | 2.15 | 4.15 | 4.05 |
| 0.62 | 0.99 | 2.91 | 2.62 | 0.29 | 1.23 | 3.13 | 0.79 | 1.47 | 1.23 | 0.61 | 1.08 | 0.95 |

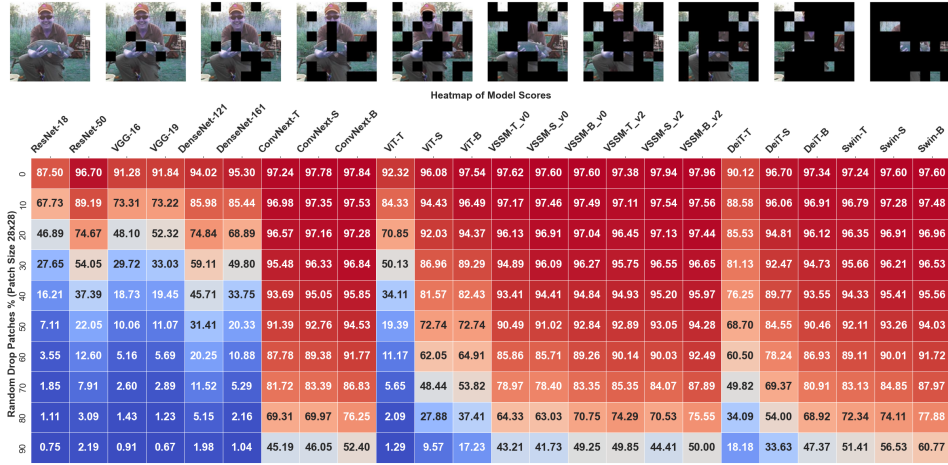


Figure 17: Top-1 classification accuracy of various architectures under random patch drop occlusions, using 28×28 patch size.

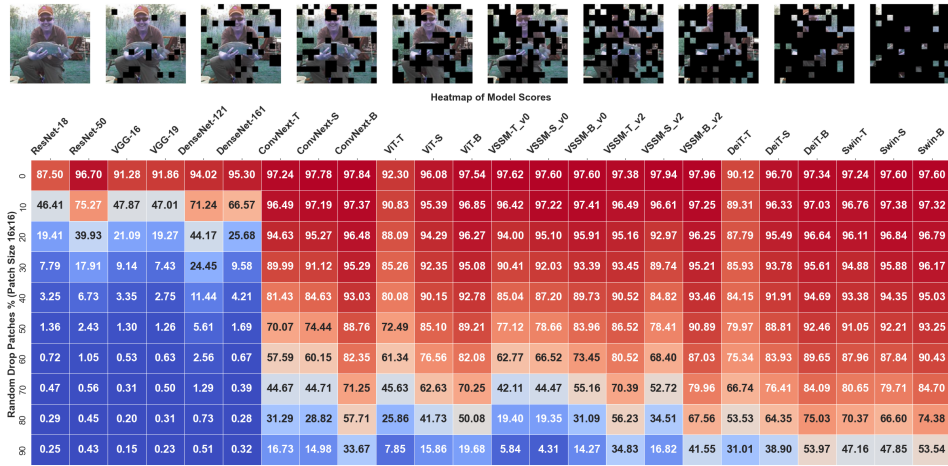


Figure 18: Top-1 classification accuracy of various architectures under random patch drop occlusions, using 16×16 patch size.

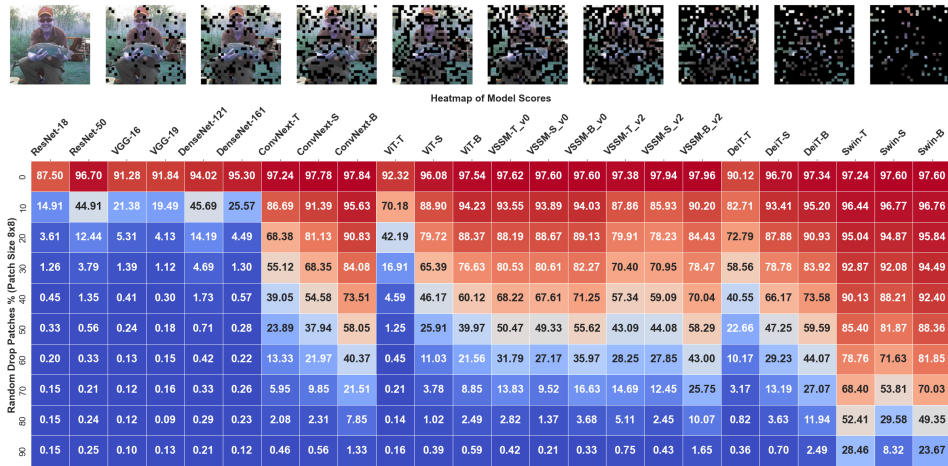


Figure 19: Top-1 classification accuracy of various architectures under random patch drop occlusions, using 8×8 patch size.

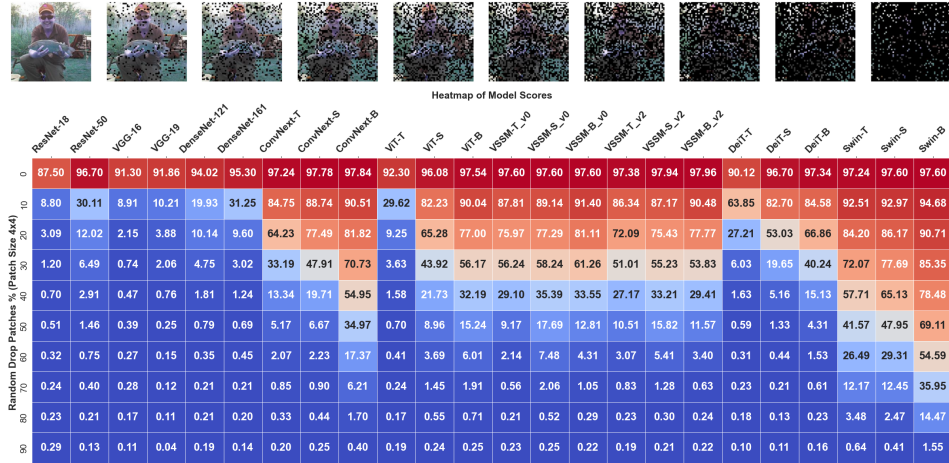


Figure 20: Top-1 classification accuracy of various architectures under random patch drop occlusions, using 4×4 patch size.

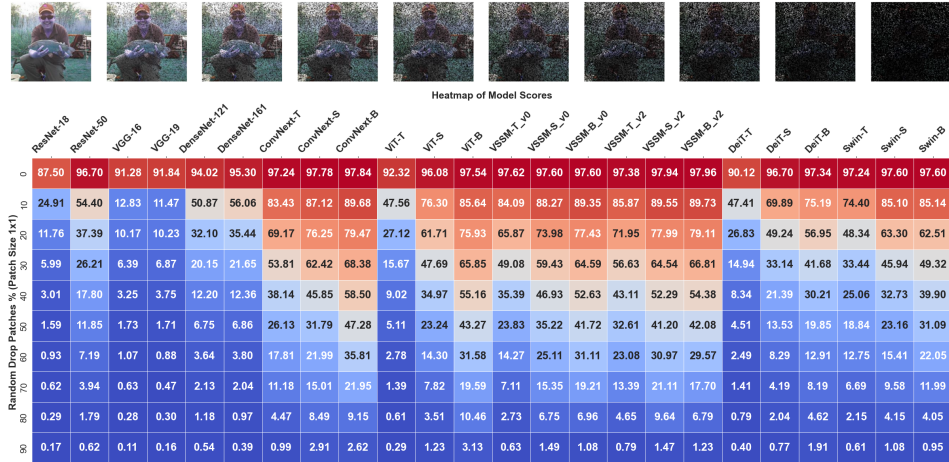


Figure 21: Top-1 classification accuracy of various architectures under random patch drop occlusions, using 1×1 patch size.

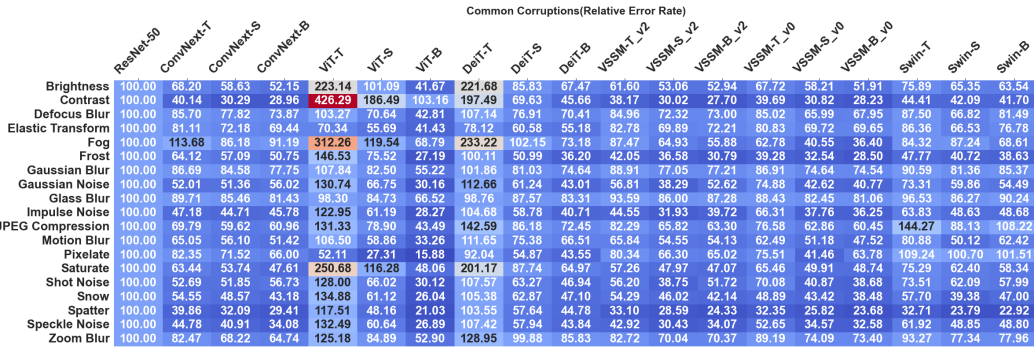


Figure 22: Relative Corruption Error values for different corruptions and architectures on ImageNet-C, with error rates relative to ResNet-50.

Table 10: Top-1 classification accuracy of various architectures on the ImageNet-E dataset [26] (left) and ImageNet-B dataset [34] (right).

| Dataset → | ImageNet-E | | | | | | | | | ImageNet-B | | | | |
|--------------|------------|-----------------|----------------|----------------------------|-----------|-------|-------|-------|-------------|------------|----------|---------|-------|-------|
| | Model ↓ | $\lambda = -20$ | $\lambda = 20$ | $\lambda = 20(\text{adv})$ | Random-BG | 0.1 | 0.08 | 0.05 | Random Pos. | Original | Original | Caption | Class | Color |
| ResNet-50 | 88.74 | 86.76 | 73.02 | 84.05 | 89.19 | 86.60 | 77.34 | 73.30 | 94.55 | 98.60 | 94.00 | 96.60 | 88.20 | 85.70 |
| VGG16 | 84.14 | 79.62 | 62.59 | 77.27 | 83.63 | 80.16 | 70.93 | 64.15 | 91.06 | 94.10 | 88.20 | 93.70 | 74.80 | 75.00 |
| VGG19 | 83.89 | 80.15 | 63.21 | 77.80 | 81.16 | 81.01 | 70.54 | 64.91 | 92.05 | 94.50 | 87.80 | 93.30 | 77.10 | 77.80 |
| DenseNet-121 | 84.93 | 81.78 | 62.36 | 79.55 | 85.15 | 81.17 | 70.08 | 64.50 | 92.78 | 96.20 | 90.20 | 95.10 | 81.10 | 80.00 |
| DenseNet-161 | 87.48 | 85.48 | 67.72 | 82.79 | 87.22 | 84.41 | 75.00 | 70.08 | 93.04 | 97.50 | 90.70 | 94.70 | 81.10 | 80.10 |
| ConvNext-T | 90.95 | 90.03 | 76.88 | 88.09 | 93.01 | 90.87 | 83.09 | 80.19 | 96.09 | 98.20 | 93.20 | 95.10 | 88.80 | 87.40 |
| ConvNext-S | 91.96 | 90.76 | 78.52 | 88.99 | 93.61 | 91.66 | 85.34 | 82.19 | 96.07 | 98.80 | 94.00 | 96.70 | 90.70 | 89.60 |
| ConvNext-B | 92.30 | 91.52 | 80.44 | 90.00 | 93.91 | 93.01 | 86.65 | 83.75 | 96.41 | 99.20 | 93.60 | 96.40 | 90.60 | 91.40 |
| ViT-T | 80.81 | 77.07 | 46.78 | 69.07 | 81.06 | 76.55 | 64.13 | 57.86 | 91.08 | 95.20 | 85.50 | 90.40 | 67.30 | 64.50 |
| ViT-S | 86.77 | 83.46 | 63.19 | 80.58 | 87.98 | 84.05 | 74.29 | 69.94 | 94.74 | 97.70 | 89.20 | 94.30 | 84.20 | 80.60 |
| ViT-B | 90.07 | 87.48 | 71.28 | 84.88 | 91.01 | 88.64 | 79.99 | 76.42 | 95.66 | 98.00 | 90.40 | 93.80 | 86.20 | 84.80 |
| DeiT-T | 80.68 | 77.21 | 51.24 | 71.83 | 80.30 | 76.83 | 65.03 | 59.54 | 89.94 | 91.60 | 86.50 | 90.50 | 73.90 | 73.20 |
| DeiT-S | 87.52 | 84.88 | 63.03 | 80.70 | 89.13 | 85.70 | 76.75 | 71.37 | 94.14 | 98.30 | 91.40 | 95.20 | 85.70 | 84.10 |
| DeiT-B | 89.66 | 86.79 | 68.77 | 84.26 | 91.10 | 89.19 | 80.31 | 77.25 | 95.38 | 98.80 | 92.30 | 96.00 | 86.70 | 84.30 |
| VSSM-T(v0) | 90.03 | 89.31 | 70.38 | 85.59 | 91.49 | 89.59 | 82.01 | 78.63 | 95.73 | 98.00 | 91.60 | 94.90 | 86.10 | 86.70 |
| VSSM-S(v0) | 90.53 | 90.76 | 73.39 | 87.78 | 93.13 | 90.71 | 83.92 | 80.42 | 96.16 | 99.10 | 92.80 | 95.40 | 89.40 | 88.50 |
| VSSM-B(v0) | 91.75 | 90.62 | 73.90 | 88.33 | 93.29 | 91.19 | 83.96 | 81.66 | 96.00 | 98.80 | 93.50 | 96.20 | 89.70 | 88.40 |
| VSSM-T(v2) | 91.15 | 89.87 | 75.18 | 87.41 | 92.09 | 91.06 | 83.66 | 79.71 | 95.84 | 98.50 | 92.20 | 96.30 | 87.20 | 86.80 |
| VSSM-S(v2) | 92.03 | 90.79 | 76.15 | 88.81 | 93.22 | 92.25 | 85.57 | 81.89 | 96.37 | 99.20 | 94.10 | 97.40 | 90.90 | 89.50 |
| VSSM-B(v2) | 92.37 | 91.27 | 77.30 | 89.11 | 93.70 | 92.64 | 86.03 | 83.62 | 96.37 | 99.10 | 94.00 | 96.50 | 90.80 | 89.80 |
| Swin-T | 90.05 | 88.83 | 71.51 | 86.19 | 91.08 | 88.94 | 79.39 | 76.49 | 95.27 | 97.90 | 91.70 | 95.30 | 85.50 | 84.00 |
| Swin-S | 90.67 | 88.86 | 73.35 | 87.25 | 91.91 | 89.68 | 81.55 | 78.81 | 96.25 | 98.30 | 91.80 | 95.50 | 86.10 | 85.40 |
| Swin-B | 91.08 | 89.96 | 75.09 | 87.87 | 92.62 | 91.22 | 83.43 | 80.65 | 95.95 | 98.60 | 92.30 | 95.60 | 89.20 | 86.70 |

Table 11: Comparison in domain generalization setting. Models trained on ImageNet are evaluated on datasets with domain shifts.

| Model ↓ | ImageNet | ImageNetV2 | ImageNet-S | ImageNet-A | ImageNet-R | Average |
|------------|----------|---------------------------|---------------------------|---------------------------|---------------------------|---------------------------|
| ConvNext-T | 81.87 | 70.67 _(-11.20) | 33.96 _(-47.91) | 10.48 _(-71.39) | 32.53 _(-49.34) | 36.90 _(-44.97) |
| ViT-T | 75.35 | 63.05 _(-12.30) | 20.88 _(-54.47) | 3.31 _(-72.04) | 20.29 _(-55.06) | 26.88 _(-48.47) |
| Swin-T | 80.91 | 69.31 _(-11.60) | 29.24 _(-51.67) | 8.93 _(-71.98) | 28.52 _(-52.39) | 34.00 _(-46.91) |
| VSSM-T(v0) | 81.92 | 70.82 _(-11.10) | 33.01 _(-48.91) | 13.56 _(-68.36) | 32.11 _(-49.81) | 37.37 _(-44.55) |
| VSSM-T(v2) | 82.28 | 71.16 _(-11.12) | 33.99 _(-48.29) | 12.08 _(-70.20) | 32.05 _(-50.23) | 37.32 _(-44.96) |
| ConvNext-S | 82.82 | 72.07 _(-10.75) | 37.16 _(-45.66) | 14.43 _(-68.39) | 35.57 _(-47.25) | 39.81 _(-43.01) |
| ViT-S | 81.40 | 69.98 _(-11.42) | 32.77 _(-48.63) | 13.09 _(-68.31) | 31.14 _(-50.26) | 36.74 _(-44.66) |
| Swin-S | 82.90 | 71.62 _(-11.28) | 31.97 _(-50.93) | 15.72 _(-67.18) | 31.93 _(-50.97) | 37.81 _(-45.09) |
| VSSM-S(v0) | 83.15 | 72.89 _(-10.26) | 38.05 _(-45.10) | 17.28 _(-65.87) | 37.05 _(-46.10) | 41.32 _(-41.83) |
| VSSM-S(v2) | 83.48 | 73.01 _(-10.47) | 36.98 _(-46.50) | 16.45 _(-67.03) | 35.75 _(-47.73) | 40.55 _(-42.93) |
| ConvNext-B | 83.75 | 73.68 _(-10.07) | 38.23 _(-45.52) | 18.16 _(-65.59) | 36.66 _(-47.09) | 41.68 _(-42.07) |
| ViT-B | 84.40 | 73.84 _(-10.56) | 43.01 _(-41.39) | 24.09 _(-60.31) | 41.03 _(-43.37) | 45.49 _(-38.91) |
| Swin-B | 83.08 | 72.09 _(-10.99) | 32.62 _(-50.46) | 17.95 _(-65.13) | 33.23 _(-49.85) | 38.97 _(-44.11) |
| VSSM-B(v0) | 83.48 | 72.97 _(-10.51) | 38.24 _(-45.24) | 18.88 _(-64.60) | 37.33 _(-46.15) | 41.86 _(-41.62) |
| VSSM-B(v2) | 83.76 | 73.22 _(-10.54) | 38.53 _(-45.23) | 18.35 _(-65.41) | 35.99 _(-47.77) | 41.52 _(-42.24) |

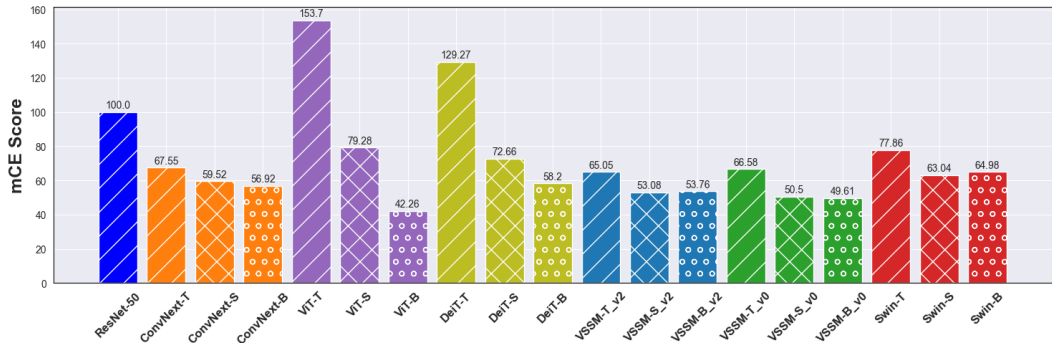


Figure 23: mCE for different corruptions and architectures on ImageNet-C, with error rates relative to ResNet-50.

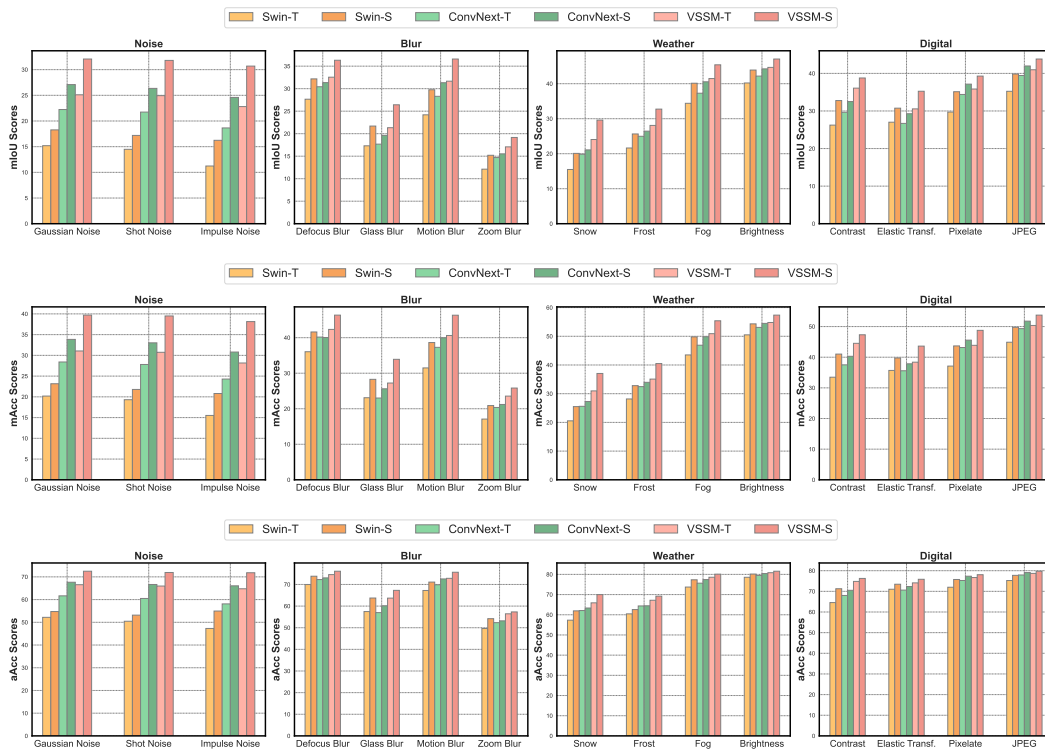


Figure 24: mIoU, mAcc, and aAcc score for different architectures on AED20k-C dataset

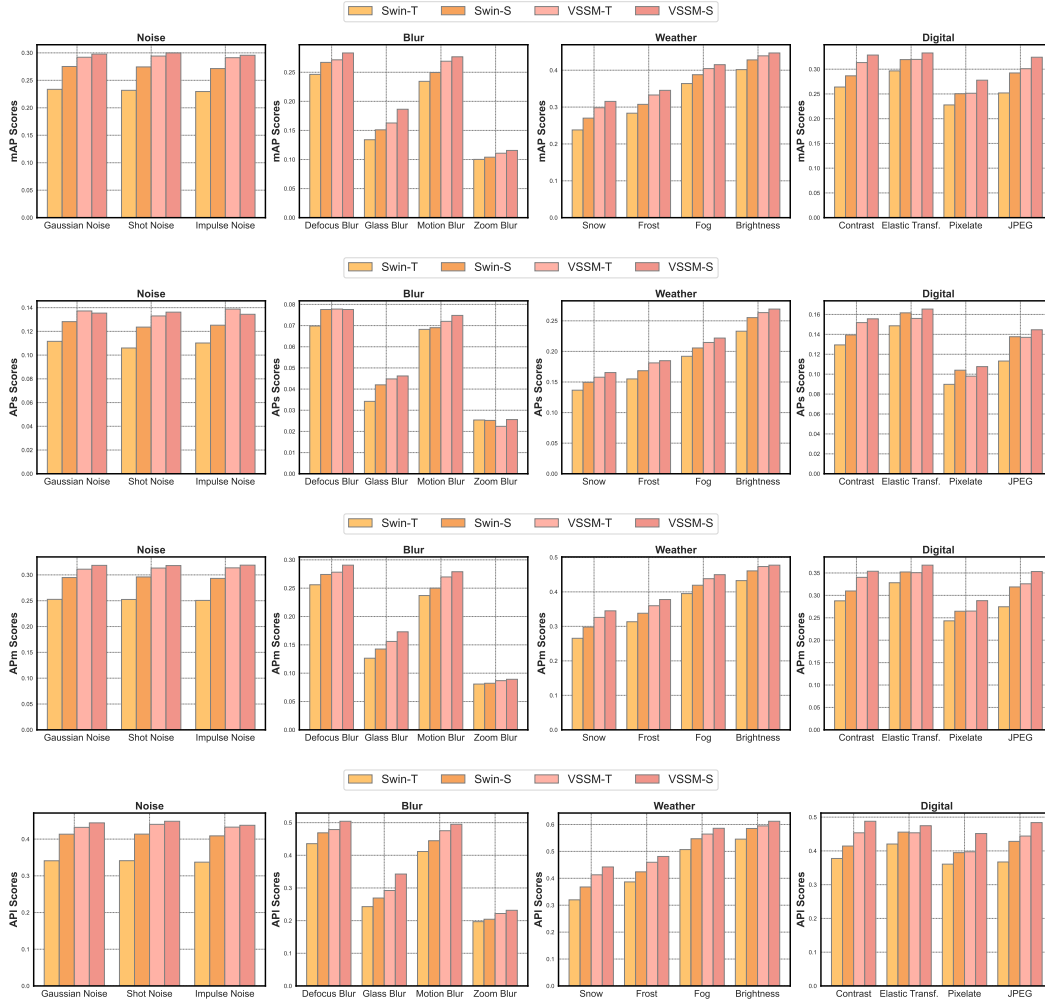


Figure 25: mAP , AP_s , AP_m , and AP_l score for different architectures on COCO-C dataset